A Frequency-Dependent Virtual Impedance Approach to Improving Stability with Grid-Forming Inverters

by

Lukas Unruh

A Thesis submitted to the Faculty of Graduate Studies of
The University of Manitoba
in partial fulfilment of the requirements of the degree of

MASTER OF SCIENCE

Department of Electrical and Computer Engineering
University of Manitoba
Winnipeg

Abstract

Grid-forming inverters have gained significant attention for their ability to improve stability in weak and islanded power systems; however, the full extent of their potential benefits for the future bulk power system remains uncertain. One potential benefit is increasing stability margins in regions affected by inverter-driven instabilities, such as series-compensated areas within the ERCOT system. This thesis explores their potential in mitigating Wind Sub-Synchronous Control Oscillations (W-SSCI) in series-compensated systems with Type-3 wind plants when a grid-forming configured battery plant is co-located with the wind plant. A novel frequency-dependent virtual impedance (FDVI) controller is proposed to improve the performance of grid-forming battery energy storage systems (BESS). Comparative analyses of grid-forming and grid-following inverters are performed to evaluate their damping capabilities.

This thesis includes the development and verification of models in EMTDC/PSCAD, incorporates impedance scanning, eigenvalue analysis, and time-domain simulations, with the objective of quantifying the minimum capacity of grid-forming BESS needed to provide stability. The results indicate that grid-forming BESS can provide substantial damping to mitigate W-SSCI, even under severe series compensation scenarios. The FDVI controller further reduces the required BESS capacity by up to 45%, demonstrating improved stability through targeted conductance tuning.

Conversely, grid-following BESS inverters are found to be unsuitable for W-SSCI mitigation because of their low admittance at sub-synchronous frequencies and susceptibility to instability under high gains or large BESS ratings. The findings strongly support the adoption of grid-forming inverters as a cost-effective solution for stability-constrained regions, offering superior damping performance compared to conventional technologies.

Acknowledgments

I would like to express my gratitude to Professor Udaya Annakkage for his guidance, support, and mentorship throughout the course of this work.

I also appreciate Electranix Corporation for their financial support and the practical experience that contributed to this research. Additionally, I acknowledge the valuable insights and advice from Andrew Isaacs, Garth Irwin, Dr. Dennis Woodford, Dr. Mukesh Das, and Kasun Samarawickrama.

Finally, thank you to my wife, my parents, and my friends for their support.

Dedication

To Andrea, Isla, and Rory.

Contents

List of Figures

List of Tables

List of Abbreviations

IBR Inverter Based Resources
GFL Grid-Following
PLL Phase-Locked-Loop
GFM Grid-Forming
NERC North American Reliability Council
HVDC High Voltage Direct Current
PSS Power System Stabilizer
BESS Battery Energy Storage System
MISO Mid-Continental System Operator
SSO Sub-Synchronous Oscillations
DFIG Doubly-Fed Induction Generator
ERCOT Electric Reliability Council of Texas
SSCI Sub-Synchronous Control Interactions
W-SSCI Wind Sub-Synchronous Control Interactions]
FACTS Flexible Alternating Current Transmission System
EMT Electro-magnetic Transient
PSCAD Power System Computer Aided Design
WTG Wind Turbine Generator
DQ Direct-Quadrature
FDVI Frequency-Dependent Virtual-Impedance
BPF Band-Pass Filter
REPC Renewable Energy Plant Controller
WECC Western Electric Coordinating Council
SMIB Single-Machine Infinite-Bus
SCR Short-Circuit Ratio
FDVA Frequency-Dependent Virtual-Admittance
LVRT Low-Voltage Ride-Through
GSC Grid-Side Converter
RSC Rotor-Side Converter
IGE Induction Generator Effect
POC Point of Connection

Chapter 1

Introduction

1.1 Background and Motivation

As the trend of renewable inverter-based resources (IBRs) displacing synchronous generation continues, the inertia and voltage-stabilizing services previously provided by synchronous generation will need to be provided by IBRs [1], [2]. The vast majority of IBRs connecting to the grid today use grid-following (GFL) technology. Conventional grid-following technology seeks to maintain a near-constant current output immediately following a system change. This involves fast measurement of system voltage using a phase-locked loop (PLL) and fast-acting current regulation loops. For this control strategy to remain stable, a relatively "stiff" AC voltage at the connection point is required to prevent excessive sensitivity of voltage to current injection by the inverter [3]. The PLL and current regulation loops together present a current-source-like characteristic to the grid. Consequently, in high-impedance networks (i.e., weak systems), the ride-through and stability performance of grid-following technology deteriorates as system voltage becomes overly sensitive to current injection.

An alternative control scheme involves maintaining a near-constant voltage magnitude and phase at the inverter terminals in the time-frame immediately following a system change (sub-transient), where the phase is constant relative to the voltage phase at some remote lo-

cation (or an ideal voltage waveform formed at the pre-event frequency). This type of control, commonly referred to as grid-forming (GFM), is usually defined by functional capabilities and desired device terminal characteristics in the linear operating range (non-current-saturated), rather than by a specific topology. The NERC White Paper [4] defines grid-forming controls as those aimed at maintaining an internal voltage phasor that is constant or nearly constant in the sub-transient time frame. After the sub-transient time frame, the grid-forming inverter adjusts the internal voltage phasor to synchronize with the grid through various controllers. Grid-forming controllers exhibit voltage-source-like characteristics, offering resilience in high-impedance networks [5]. Historically, grid-forming inverters were primarily used in microgrids, islanded systems, and specialized HVDC applications such as offshore wind plants. However, since approximately 2018, there has been growing interest in adopting grid-forming technology in bulk power systems [6]. This potential widespread adoption in bulk power systems, not limited to regions of weak system strength and inertia, invites exploration of additional stabilization benefits grid-forming inverters could provide. One such capability is stabilizing unstable or poorly damped system modes—a task traditionally handled by power system stabilizer (PSS) controllers on synchronous machines. Conventional power systems, dominated by synchronous resources, typically exhibit well-defined electromechanical modes in specific frequency ranges (e.g., 0.7–2.0 Hz for local modes and 0.1–0.3 Hz for inter-area modes) [7]. By contrast, power systems with increasing IBR penetration may experience oscillatory modes over a broader frequency spectrum, requiring faster and more dynamic mitigation solutions.

A notable example of sub-synchronous oscillations (SSO) involving inverters is the interaction between Type-3 Doubly Fed Induction Generator (DFIG) [8] wind turbines and series-compensated transmission networks, as observed in the ERCOT system [9]. These oscillations, characterized by rapid growth and frequencies between 6 Hz and 30 Hz in phase currents, have been documented in multiple real-world events [10]. The frequency and damping of such oscillations vary significantly depending on network and operating conditions.

This specific instability, termed Sub-Synchronous Control Interaction (SSCI) in [11] and more recently as Wind-SSCI (W-SSCI) in [12], imposes significant commercial constraints in regions with series compensation. W-SSCI represents an ideal challenge for testing grid-forming controls due to the frequency variability and potential instability of involved modes.

1.2 Thesis Focus and Scope

This thesis examines a practical scenario involving a new Battery Energy Storage System (BESS) co-located with a grid-following Type-3 wind plant connected to a stability-constrained, series-compensated network. Such hybrid plants, which share a connection point, are becoming increasingly common [13]. They allow generator owners to shift energy output to better align with load curves, enhancing project profitability, and bypass long interconnection study queues when maximum net power injection ("interconnection rights") does not increase, as observed in the MISO system [14].

We propose implementing grid-forming controls for the battery inverters as a robust, cost-effective approach to mitigate stability constraints. While alternative mitigation strategies for W-SSCI and SSO exist—such as control tuning, supplementary damping controllers, FACTS devices [12] [15] [16], or implementing grid-forming controls on Type-3 wind turbines [17]—a comprehensive comparison of these methods is beyond the scope of this thesis. If grid-forming inverters can relax stability constraints, they may represent the most cost-effective option since the cost difference between grid-following and grid-forming inverter technology is smaller than the costs of modifying existing wind plants, the grid, or supplemental FACTS devices. Battery inverters were specifically selected for this analysis because grid-forming technology is commercially available for these systems. Additionally, battery inverters avoid challenges faced by other resource types, such as DC-side energy availability constraints in PV systems and mechanical stress concerns in wind turbines.

Conventional power systems rely on power system stabilizers (PSS) to mitigate prob-

lematic modes at relatively low frequencies. Grid-forming inverters have the flexibility to replicate PSS behavior, as demonstrated in [18], but are not constrained by the typical PSS structure, as their controls operate nearly instantaneously. However, PSS schemes often influence the inputs to the power synchronization loop of grid-forming inverters. The power synchronization loop typically has a strong impact on performance of the inverter at low frequencies, and does not have much effect at higher sub-synchronous frequencies. This limitation reduces the effectiveness of PSS-based schemes in mitigating W-SSCI oscillations, which tend to occur at higher frequencies.

An alternative to traditional PSS schemes for improving sub-synchronous performance is enhancing the device's frequency-domain impedance characteristics through virtual impedance. Virtual impedance schemes for inverter-based resources (IBRs) are well-established and are primarily applied to improve current sharing in microgrids or distributed generation systems [19] [20] [21], as well as to limit fault currents in grid-forming inverters [21]. However, there has been limited investigation into the use of virtual impedance for damping sub-synchronous phenomena, such as W-SSCI, in bulk power systems. The virtual impedance method proposed in this thesis introduces a frequency-dependent characteristic to the virtual impedance using band-pass filters. This approach modifies the inverter's impedance over targeted frequency ranges, enabling more current headroom for the inverter to supply other grid services. Additional details about virtual impedance and its application in this study are provided in Chapters 2 and 4.

This thesis explores the damping capabilities of grid-forming inverters and provides a benchmark comparison with the performance of a grid-following inverter. While the comparison offers useful context, it is not exhaustive, as the primary focus of the study is on grid-forming inverters. Although several modifications could potentially enhance the performance of the grid-following inverter model used in this analysis, implementing such improvements was beyond the scope of this research.

The primary focus of this thesis is on the small-signal performance of the system. Small-

signal performance was assessed using eigenvalue analysis, where the system's state-space model was obtained through impedance-scanning techniques. Additionally, a limited Electro-Magnetic Transient (EMT) time-domain analysis was conducted in PSCAD to verify the small-signal analysis and to assess potential large-signal impacts introduced by controller modifications. However, this was not a comprehensive time-domain analysis, as fault-recovery dynamics were not the main focus of the research.

1.3 Organization of Thesis

The remainder of the thesis is organized into the following chapters. Chapter 2 discusses the development and parameterization of the device models used in the analysis, including the virtual impedance modifications. Chapter 3 introduces the test system which was used to assess the performance of the grid-forming inverters. In Chapter 4, an overview of the impedance-scan methodology is provided. This chapter also includes a description of the optimization technique which was used to parameterize the virtual impedance controller. Chapter 5 covers the methodology and results pertaining to the full system analysis, including the eigenvalue analysis and time-domain simulations. Chapter 6 present the conclusions of the thesis and suggestions of future work in this research area.

Chapter 2

Model Development

The analysis performed in this thesis utilized three different device models. First, a grid-forming BESS model was developed in PSCAD program to test the performance of the proposed control changes. Next, a grid-following variation of the BESS model was developed to benchmark the performance of the grid-forming BESS. Finally, a Type-3 wind turbine generator (WTG) plant model was used as part of the test network. This model, developed by the PSCAD software authors and available on the PSCAD website [22], was utilized with minor modifications for this analysis. Further details regarding the development and use of these models are provided below. For each of these three models, time-domain simulation tests were performed to verify the basic fault response of the devices.

2.1 BESS Inverter Electrical Model

The single-line diagram of the BESS electrical representation considered in this analysis is shown in Figure 2.1. The same electrical representation is used for both the grid-forming and grid-following BESS models. An average-value method [23] was employed to interface the inverter with the system. This method ignores the effects of high-frequency power electronic gate switching but runs much faster than a full switching model. This approximation was deemed acceptable, as the primary focus is the behavior of the BESS at sub-synchronous

frequencies.

The inverter is connected to the system through an LCL filter, parameterized as shown in Table 2.1. The LCL filter was designed approximately following the process described in [24]. The switching frequency assumed for the calculation was 4 kHz, and the resonant frequency of the LCL filter was set to 2.5 kHz. The per-unit capacitance of C_f was set to 0.015 pu, while the inverter-side inductor L_f was set to 0.12 pu. The resistor in series with the capacitor, R_f, was set to 0.42 pu to provide damping at the resonant frequency. The inverter transformer forms the grid-side inductor R_C of the filter and is set to 0.058 pu. The inverter transformer is a scalable device, enabling the rating of the aggregate BESS model to be adjusted as needed.

On the DC side, the battery is modeled as an ideal voltage source behind an equivalent internal resistor, where the resistor was rated so that the full-load voltage drop across the resistor is limited to 3%. This represents a simple model of a direct-connected battery, which is common for grid-scale BESS plants, without any additional DC-DC converters between the battery and the inverter. A DC capacitor rated to store 5 kJ per 1 MW inverter was included in parallel to the equivalent battery model. Battery constraints, such as state of charge and any DC current limitations, were not modeled. These assumptions are considered acceptable for a direct-connected battery system because the primary focus in this thesis is the small signal performance of the BESS when it is not operating at or near an SOC limit. Given that the storage durations of grid-scale BESS plants is typically on the scale of hours, it is reasonable to assume that SOC would have negligible impact on the phenomena considered in this research. Investigation into performance of the BESS when operating at the limits is left for future work.

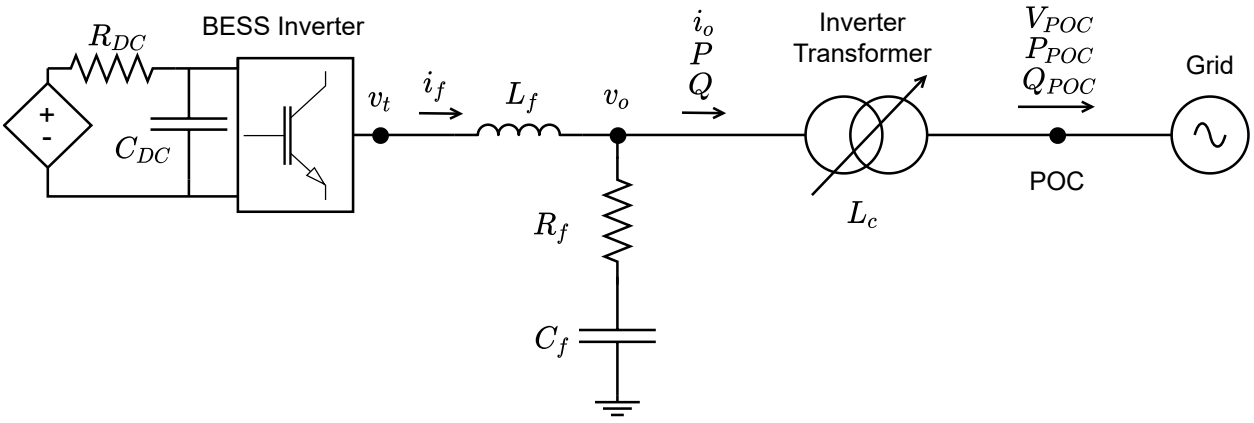

Figure 2.1: BESS Inverter's Electrical Representation

2.2 Grid-Forming Inverter Control Design

Grid-forming inverter control is an active research area, which has produced many proposed control topologies. Multiple different approaches are described in [25], [26], and [27]. The control diagram of the grid-forming BESS inverter considered in this thesis is shown in Figure 2.2. A key component of the grid-forming inverter is the primary control loop, which synchronizes the inverter internal angle/frequency and voltage magnitude with the external grid without the use of a phase-locked-loop. The active power component of the primary control loop determines the phase angle of the desired terminal voltage phasor θ. This is achieved using a virtual machine approach, which incorporates a simplified swing equation with an added damping term to compute the virtual machine's speed and rotor angle. The acceleration constant, T_a, and damping coefficient, D, of the swing equation were selected based on time-domain trial-and-error testing which showed the values of 2 s and 66.67, respectively, to provide stable results in both a weak grid and a stiff grid. Note that the value of 66.67 for the damping coefficient results in a power-frequency droop of 1.5%. This is less than the typical power-frequency droop requirement of 5%. To correct for this, a slow outer-loop plant-level controller was added to control to a droop of 5%.

The reactive power portion of the primary control loop is responsible for generating the magnitude of the desired terminal voltage phasor. It does this through a direct droop

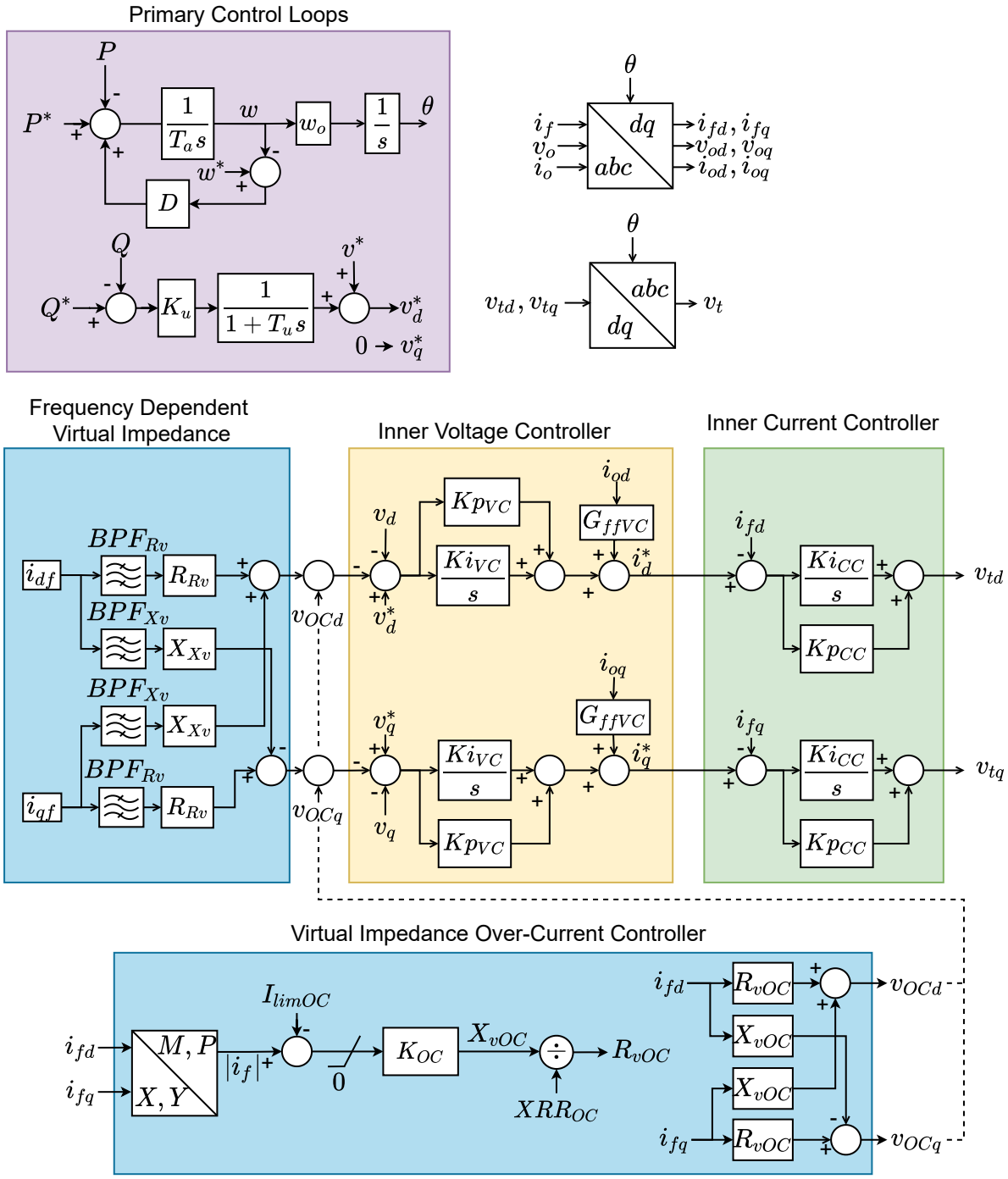

Figure 2.2: Control Diagram of Grid-Forming BESS Inverter, Including the Frequency-Dependent Virtual Impedance

control method, which multiplies the error between the reference reactive power Q^* (which was nominally set to 0) and the measured reactive power Q by the voltage-droop constant K_u, which is set to 0.05 pu. The result is then passed through a single-pole lag function (time constant T_u) in order to make the reference voltage magnitude less sensitive to fast changes in reactive power, which was found to increase stability. Additionally, an external voltage reference V^* is injected at the end of this loop to allow for a slow outer-loop plant controller to adjust for reactive losses. It is important that the primary control loop response time is longer than the sub-transient period, so that they do not interfere with the grid-forming inverters ability to maintain a constant or near-constant internal voltage phasor during that time-frame.

The primary control loops result in a reference voltage phasor (magnitude and angle) for the voltage at the midpoint of the LCL filter. The magnitude of this phasor becomes the D-axis voltage reference (V_d^*), and the Q-axis voltage reference is set to 0. These V_d^*, V_q^* reference signals are then used as inputs to a cascaded controller structure which controls the voltage and current outputs of the converter in the DQ domain. The cascaded control structure includes voltage and current feed-forward terms, and may include DQ decoupling terms. The outputs of the PI controllers are then transformed into the instantaneous voltage v_t which is applied at the inverter average value source interface. The cascaded control structure allows for the control of the magnitude of the output current by applying limits to the current reference commands. The current control loop was tuned by applying a step change in current reference and optimizing the current output response for minimal response time, settling time, and overshoot. Selecting 2.0 and 30.0 for the Kp_{CC} and Ki_{CC} gains, respectively, resulted in a rise time of 0.4 ms, pct overshoot of 15%, and settling time of 10 ms, which was considered acceptable. The frequency of oscillation was 380 Hz and the damping ratio was 0.09. Note that the rise time and settling time could have been further reduced, at the expense of higher overshoot and reduced an increased region of negative damping in the sub-synchronous frequency impedance characteristic. The voltage control

structure was tuned so to have a response time 10 times slower than that of the current control loops, with some further adjustments made to the PI gains based on time-domain performance and sub-synchronous frequency impedance.

2.2.1 Grid-Forming Inverter Frequency-Dependent Virtual Impedance

In an effort to improve the sub-synchronous damping of the grid-forming inverter, a modified virtual impedance approach was implemented. Virtual impedance has many different uses, as described in Chapter 1. The concept of virtual impedance is explained in Figure 2.3. Virtual impedance methods typically calculate the voltage drop across a fictitious series impedance, $Z_{virtual}$, caused by the output current. This calculated voltage drop is then subtracted from the original reference voltage v_0^* to produce a new reference voltage v^*. The inner voltage and current control loop then works to implement the desired modified reference voltage at the inverter terminals. This effectively causes the inverter to act as if there was an additional impedance $Z_{virtual}$ between the device terminals and the grid.

The modified virtual impedance loop considered in this thesis consists of passing the currents used in the virtual impedance loop through a band-pass filter before calculating the new voltage reference, resulting in a frequency-dependent virtual-impedance (FDVI) characteristic. The benefit of applying a band-pass filter (BPF) is that the control response resulting from the FDVI is constrained to a specific frequency range, leaving more current capacity available for additional services provided by the grid-forming BESS, such as voltage support, frequency support, energy arbitrage, etc. The BPF is of the form noted in Eq. (2.1).

$$\frac{Y(s)}{X(s)} = \frac{G_{BPF}\frac{s}{\omega_c}}{1 + \frac{1}{Q}\frac{s}{\omega_c} + \frac{s}{\omega_c}^2} \tag{2.1}$$

The BPF of the virtual resistance path was configured differently from the BPF of the virtual reactance path, however a quality factor, Q, of 3 and a gain of 1 was common between

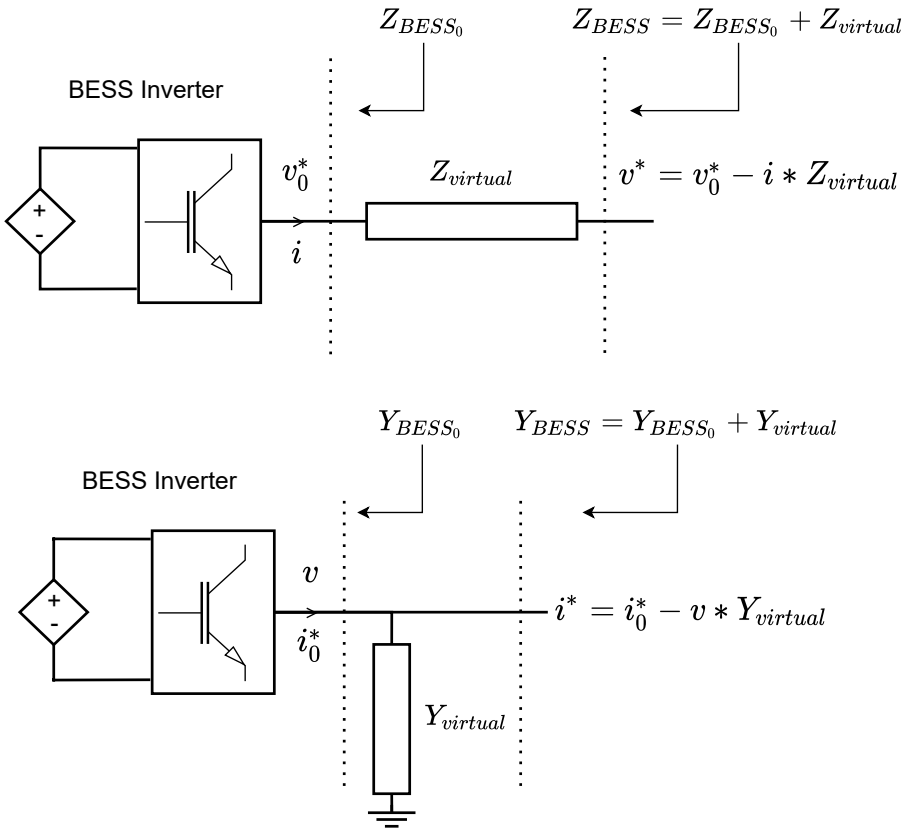

Figure 2.3: Concept of Virtual Impedance/Admittance

the two filters. The quality factor of 3 was selected because it was found to strike a balance between a wide filter that will affect the inverter impedance at a wide range of frequencies, which is undesirable, and a filter that is tightly tuned to a particular frequency, whose performance would be sensitive to small changes in the frequency of critical system modes. Further optimization of the quality factor is left for future research. The values of the BPF center frequency (ω_c), virtual resistance, and virtual reactance were determined as part of optimization method outlined in Chapter 4. Figure 2.4 shows an example of the frequency response of the filter with quality factor of 3, gain of 1, and center frequency set to 30 Hz.

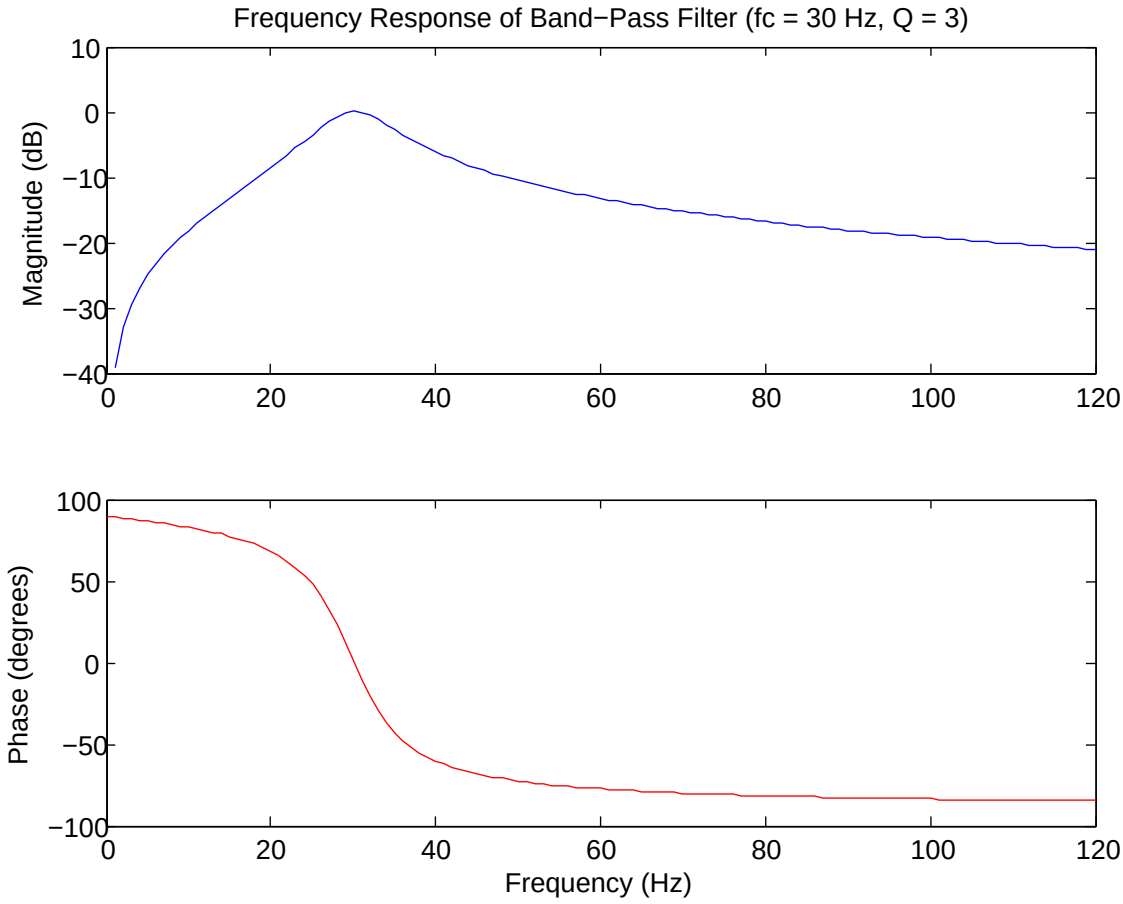

Figure 2.4: Band-Pass Filter Frequency Response

2.2.2 Grid-Forming Inverter Current Limiting

Appropriate current limiting in grid-forming inverters should stop current flow from exceeding ratings of switching devices, and maintain the stability of the grid-forming inverter internal quantities during and after the fault. In this thesis, the primary focus was the small-signal behavior of the grid-forming inverter, however a current limiting strategy was included for completeness of the model. There are many possible ways to implement current limiting, including virtual impedance, switching-level limiting, current reference saturation, and direct modification of the output voltage phasor [28], [29]. The current limiting strategy used in the grid-forming model was the virtual impedance method outlined in [21]. This

method implements an adaptive virtual impedance, whose magnitude is determined by the magnitude of output current that is above a certain threshold, as shown in the bottom of Figure 2.2. The virtual impedance is then applied by subtracting the voltage drop across the impedance from the voltage references. Values of control parameters for this controller are provided in Table 2.1.

Table 2.1: Table of Grid-Forming BESS Inverter Control Parameters

Description	Symbol	Value
Primary Control Acceleration Constant	T_a	2 s
Primary Control Damping Coefficient	D	66.67 pu
Primary Control Voltage Droop	K_u	0.05 pu
Primary Control Voltage Time Constant	T_u	1 s
Inner Voltage Control Proportional Gain	Kp_{VC}	0.3 pu
Inner Voltage Control Integral Gain	Ki_{VC}	1.5 pu
Inner Voltage Control Feed-Forward Gain	$G_{ff\,VC}$	1.0 pu
Inner Current Control Proportional Gain	Kp_{CC}	2.0 pu
Inner Current Control Integral Gain	Ki_{CC}	30.0 pu
FDVI Band Pass Filter Gain	G_{BPF}	1
FDVI Band Pass Filter Q	Q_{BPF}	3
FDVI Virtual Resistance	R_{Rv}	0.088 pu
FDVI Virtual Reactance	X_{Xv}	-0.128 pu
FDVI Virtual Resistance BPF Center Frequency	$\omega_{c\,Rv}$	41 Hz
FDVI Virtual Reactance BPF Center Frequency	$\omega_{c\,Xv}$	49 Hz
Virtual Impedance Over-Current Gain	K_{OC}	1.75 pu
Virtual Impedance Over-Current Current Limit	$IlimOC$	1.2 pu
Virtual Impedance Over-Current X by R Ratio	XRR_{OC}	2.5
LCL filter values (per-unit on 1 MVA base)	L_c	0.058 pu
	L_f	0.015 pu
	C_f	0.12 pu
	R_f	0.42 pu
DC Capacitor	C_{DC}	10 mF
DC Resistor	R_{DC}	0.05 ohm

2.2.3 Outer-Loop Voltage and Frequency Controllers

Outer-loop voltage and frequency controllers were added to the BESS inverter model such that the plant-level output can be precisely controlled at slower time-frames. These con-

trollers approximately follow the renewable energy plant controller model developed by WECC [30], however for the purposes of the grid-forming BESS model, the voltage controller outputs a voltage reference for the inner voltage-control loop rather than a Q reference. Figure 2.5 shows these control loops. Values of control parameters are provided in Table 2.2

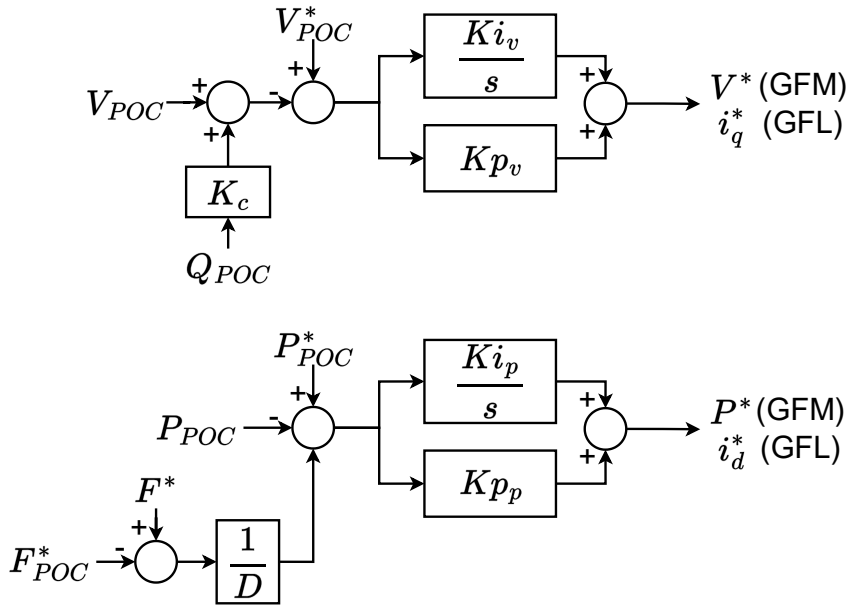

Figure 2.5: Control Diagram of BESS Plant Controller

Table 2.2: Table of BESS Plant Controller Control Parameters

Description	Symbol	Value
Plant Controller Voltage Proportional Gain	Kp_v	0.1 pu
Plant Controller Voltage Integral Gain	Ki_v	1.0 pu
Plant Controller Voltage Droop	K_c	0.05 pu
Plant Controller Frequency Proportional Gain	Kp_p	0.01 pu
Plant Controller Frequency Integral Gain	Ki_p	2.0 pu
Plant Controller Frequency Droop	D	0.05 pu

2.2.4 Grid-Forming Inverter Time-Domain Verification

Time-domain tests were performed for all dynamic models in PSCAD to verify that the models can initialize correctly, can recover from a 3-phase fault in a stable manner, and that fault current is limited. These tests were performed with the models operating into a simple single-machine-infinite-bus (SMIB) system which is configured to be relatively weak. This type of isolated model testing provides a degree of confidence in the model's robustness and performance when used in more complex systems. The test system contains a fault component and a configurable AC source whose voltage magnitude and phase could be adjusted. The SMIB source strength was configured with a short-circuit-ratio of 2.5, and an X/R ratio of 5 to represent a typical relatively weak system.

In addition to fault ride-through testing, the grid-forming inverter's voltage-source behavior was verified by applying step changes to the SMIB source voltage phase and magnitude, which is one of several ways to verify this behavior. Figure 2.7 shows the response to a 10 degree increase in source voltage phase angle at 5 s, and a 0.1 pu decrease in source voltage magnitude at 6.5 s. The inverter has an immediate reduction in active power in response to the phase angle jump, indicating that the internal phase angle is held constant in the transient time frame. Likewise, the reactive power out of the inverter immediately increases upon grid voltage magnitude decrease, indicating a constant inverter voltage magnitude.

Figure 2.7 shows the response of the inverter to a low-impedance 3-phase fault. The current during the fault was limited by the current limiting strategy, however the post-fault recovery dynamic could be improved. During the fault, the active power primary control loop is winding-up because the measured power output is much less than the reference, which results in the internal phase angle advancing past the system phase angle. This causes the swing in active power when the fault is removed. There is also a dip in reactive power at fault clearing which leads to an under-voltage. This dip was determined to occur due to wind-up effects introduced by the current-limiting virtual impedance. Avoiding these

types of fault wind-up / re-synchronization issues is currently an active research area and many solutions have been proposed. As this paper focuses on the small-signal aspects of the inverter, optimizing the primary control loop and current limiting strategy to avoid wind-up effects was left for a future effort. These tests verify that the grid-forming inverter model initializes correctly, limits the fault current, and recovers from the fault in a stable manner.

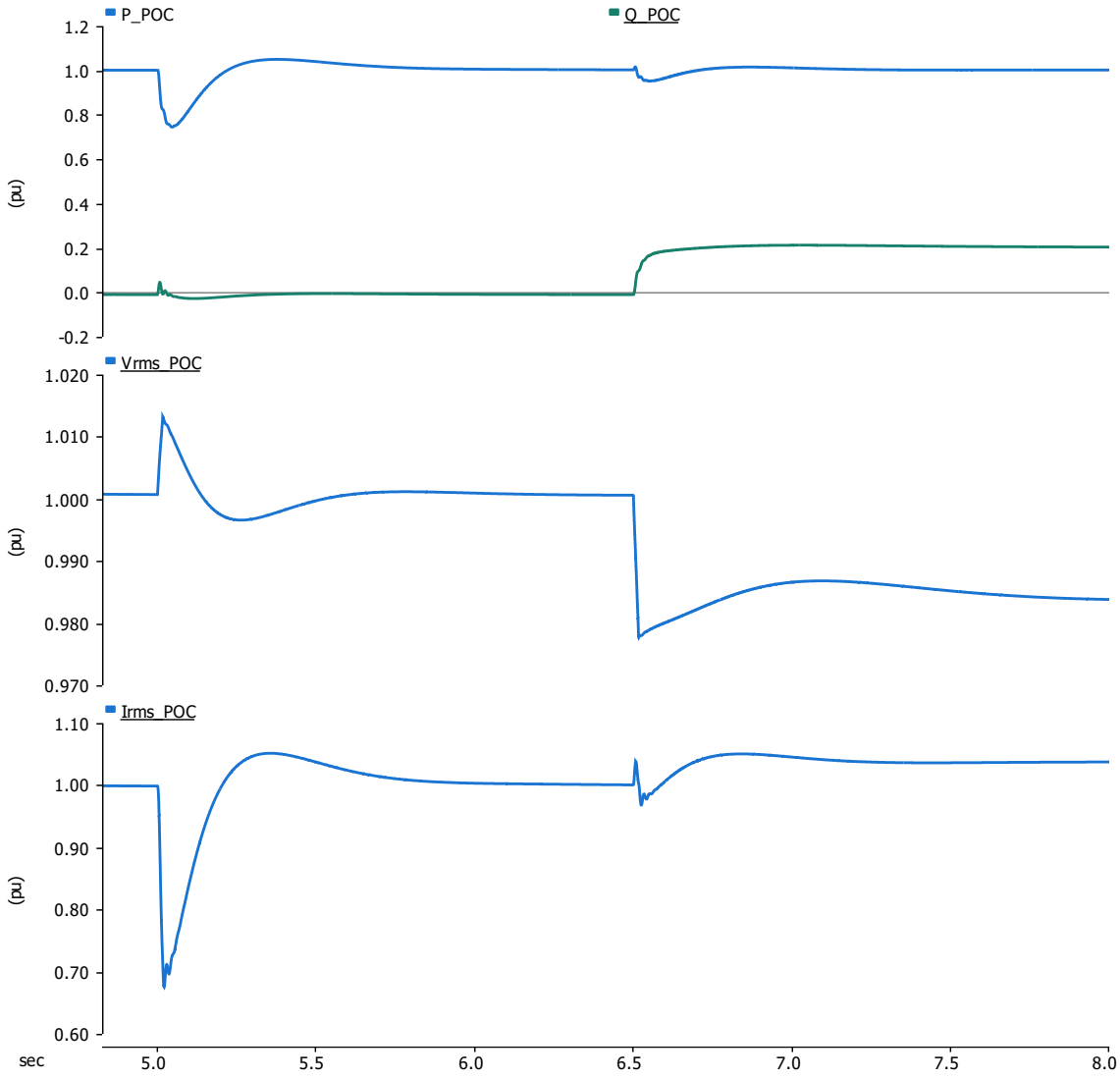

Figure 2.6: Grid-Forming BESS Inverter: Voltage Source Phase and Magnitude Step Response

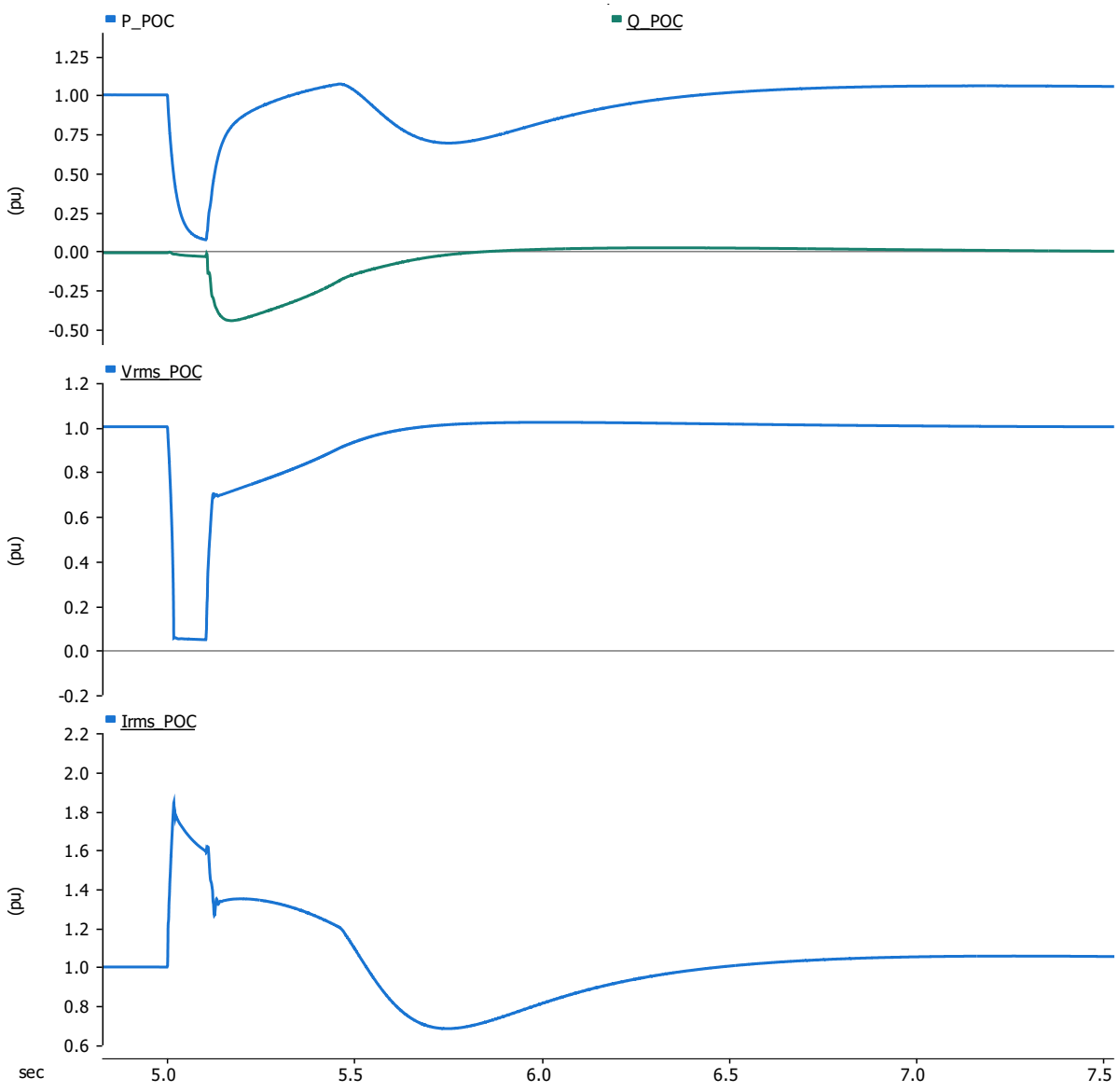

Figure 2.7: Grid-Forming BESS Inverter: Fault Response

2.3 Grid-Following Inverter Control Design

A conventionally-controlled grid-following BESS model was also developed in order to benchmark the performance of the grid-forming BESS. The same current control loops and slow outer-loop voltage and frequency control loops were used in the grid-following model, however the outputs of the outer loop controls were used directly as current references in the current control loops. Additionally, a phase-locked-loop (PLL) [31] was used to track the

grid voltage angle, which was then used to transform all ABC quantities into DQ quantities and vice-versa. The PLL used in the model was a stationary-frame PLL. The full control diagram of the grid-following inverter is shown in Figure 2.8, and the control parameter values and descriptions are shown in Table 2.3.

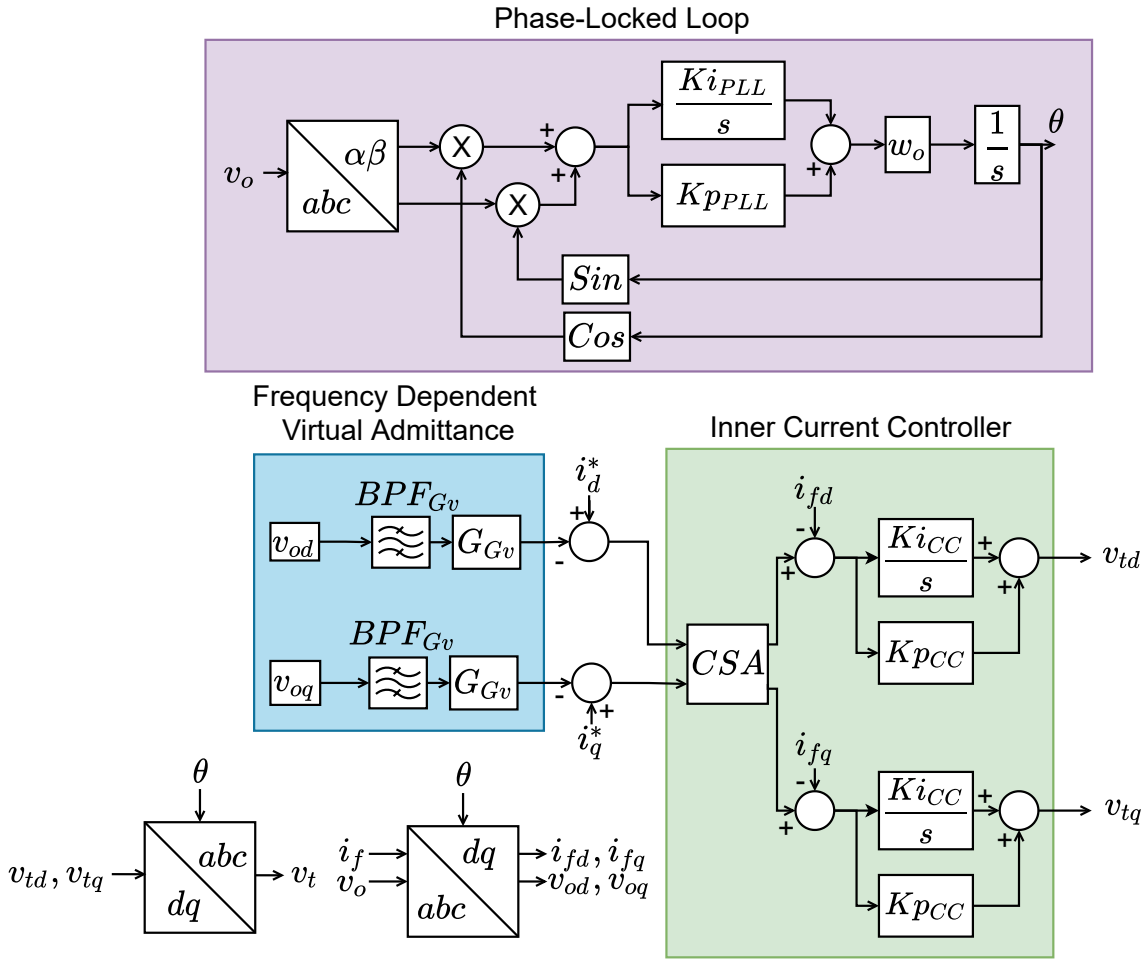

Figure 2.8: Control Diagram of Grid-Following BESS Inverter

The impedance of the grid-following BESS inverter was virtually modified using a similar approach as was used for the grid-forming inverter. Since the grid-following inverter does not include an inner voltage control loop where a virtual voltage drop could be applied across a fictitious series impedance, a virtual admittance approach was adopted instead. This method incorporates the current flowing through a fictitious shunt admittance, driven by the measured voltage, into the current reference supplied to the inner current control

loop. This controller is referred to a frequency-dependent virtual-admittance (FDVA). This concept is shown in Figure 2.3.

This grid-following BESS model developed for this thesis is relatively simple. It does not have all of the control functions found in modern inverters, such as low-voltage ride-through and power-frequency controllers. It was designed primarily to provide insight into the general small-signal performance of the grid-following topology.

Table 2.3: Table of Grid-Following BESS Inverter Control Parameters

Description	Symbol	Value
Phase-Locked-Loop Proportional Gain	Kp_{PLL}	1.5 pu
Phase-Locked-Loop Integral Gain	Ki_{PLL}	6.0 pu
Inner Current Control Proportional Gain	Kp_{CC}	2.0 pu
Inner Current Control Integral Gain	Ki_{CC}	30.0 pu
FDVA Band Pass Filter Gain	G_{BPF}	1
FDVA Band Pass Filter Q	Q_{BPF}	3
FDVA Virtual Conductance	G_{Gv}	2.42 pu
FDVA Virtual Conductance BPF center frequency	$\omega_{c\,Gv}$	34.5 Hz

2.3.1 Grid-Following Inverter Time Domain Verification

A fault response test was performed for the grid-following inverter to verify the ride-through and recovery behavior in PSCAD. The test system is the same SMIB system which used to test the grid-forming inverter. Figure 2.7 shows the response of the inverter to a low-impedance 3-phase fault when the SMIB source was configured with a short-circuit-ratio of 2.5. The current during the fault was limited by the current controller, and there is a transient at fault clearing as the inverter PLL re-synchronizes. This test verifies that the grid-following inverter model initializes correctly, limits the fault current, and recovers from the fault in a stable manner.

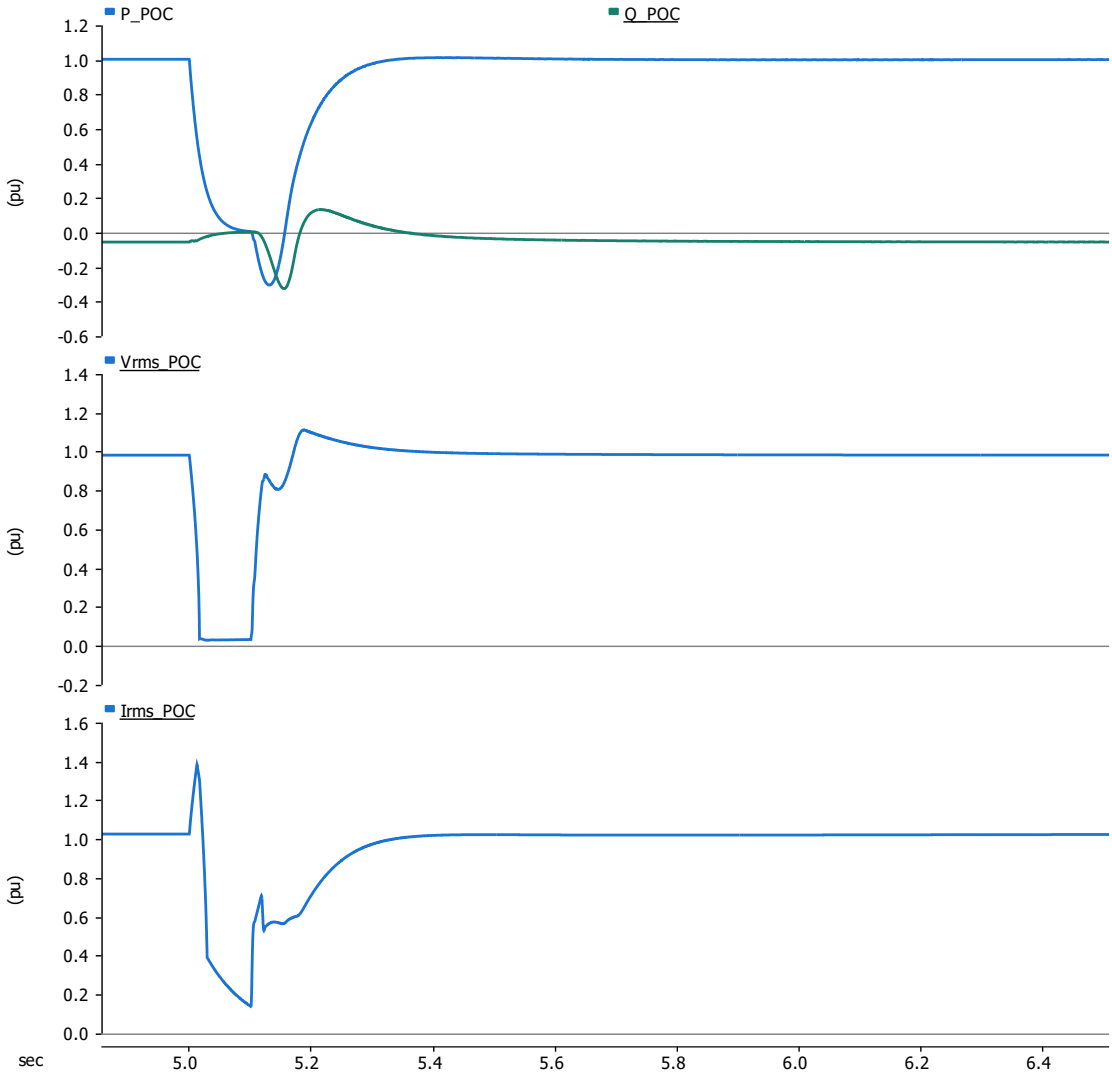

Figure 2.9: Grid-Following BESS Inverter: Fault Response

2.4 Wind Plant Model

The wind plant is using generic Type-3 wind turbine model. The model which was used in this analysis is publicly available [22]. A thorough discussion of the model development and verification process can be found in [32], where the model authors particularly mention that the model is suitable for W-SSCI study. The model ratings were modified to match the test system, otherwise the model was not substantially changed from the public version.

Note that this model did not have any sub-synchronous damping controllers included, which are commonly employed by commercial-grade turbines to mitigate instability risk in series-compensated systems. The full details of the wind turbine model can be found online [22]. The electrical model of the WTG and a simplified control diagram are shown in Figure 2.10. The full model contains many ride-through features that are not detailed here for brevity. Table 2.4 lists the values of key model control parameters.

Table 2.4: Table of Type-3 WTG Model Key Control Parameters

Description	Symbol
GSC PLL Proportional Gain	500 pu
GSC PLL Integral Gain	2000 pu
GSC DC Voltage Control Proportional Gain	2 pu
GSC DC Voltage Control Integral Gain	100 pu
GSC Converter Q Control Proportional Gain	1 pu
GSC Converter Q Control Integral Gain	10 pu
GSC i_d Current Control Proportional Gain	2 pu
GSC i_d Current Control Integral Gain	100 pu
GSC i_q Current Control Proportional Gain	2 pu
GSC i_q Current Control Integral Gain	100 pu
RSC PLL Proportional Gain	200 pu
RSC PLL Integral Gain	2000 pu
RSC WTG P Control Proportional Gain	2 pu
RSC WTG P Control Integral Gain	50 pu
RSC WTG V Control Proportional Gain	0.5 pu
RSC WTG V Control Integral Gain	20 pu
RSC WTG Q Control Proportional Gain	2 pu
RSC WTG Q Control Integral Gain	20 pu
RSC i_d Current Control Proportional Gain	2 pu
RSC i_d Current Control Integral Gain	40 pu
RSC i_q Current Control Proportional Gain	2 pu
RSC i_q Current Control Integral Gain	100 pu

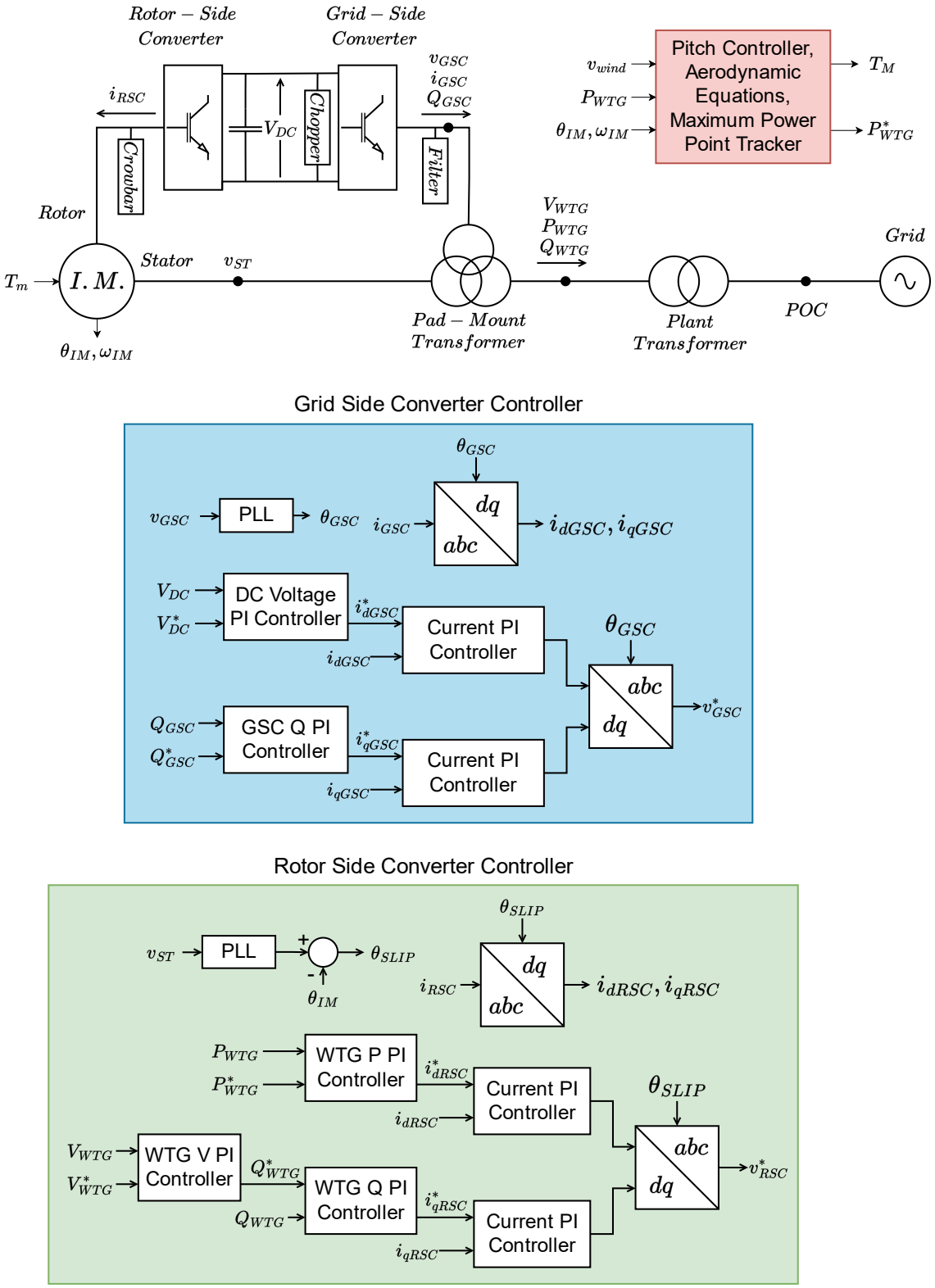

Figure 2.10: Electrical and Control Diagram of Type-3 WTG

2.4.1 Wind Plant Time-Domain Verification

A fault response test was performed on the wind plant to verify the ride-through and recovery behavior in PSCAD. The test system is the same SMIB system as was used to test the grid-forming inverter. Figure 2.11 shows the response of the wind plant to a deep fault when the SMIB source was configured with a short-circuit-ratio of 2.5. This test verifies that the wind plant model initializes correctly, and recovers from the fault in a stable manner.

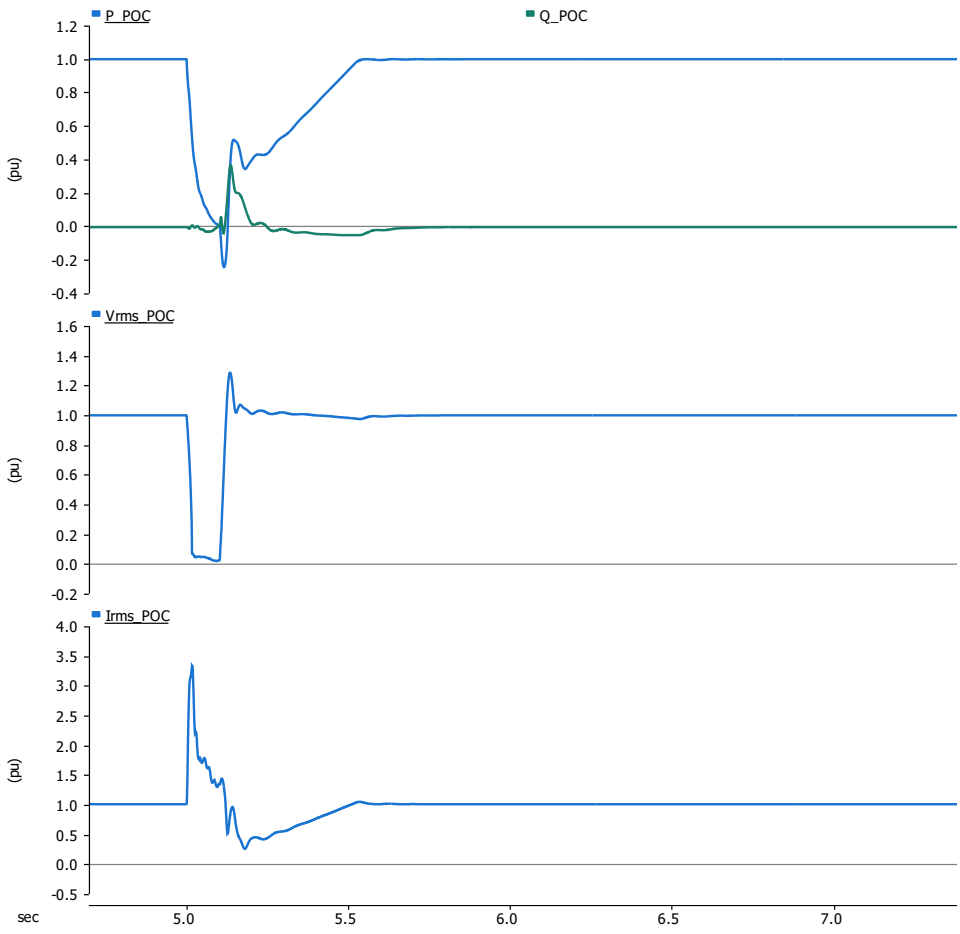

Figure 2.11: Type-3 WTG: Fault Response

Chapter 3

Test System

3.1 Test System Selection

The test system considered in this analysis consists of an aggregate BESS inverter connected in parallel with a 450 MW wind plant, where the wind plant is using generic Type 3 wind turbines. The rating of the BESS is varied as part of the analysis. The plant is connected into a 345 kV system through a long transmission line which contains a series capacitor at its midpoint, with a system equivalent at the remote end. This system is characteristic of a remotely-located wind farm which is transferring power over a long distance to a load center. Figure 3.1 shows this test system. Note that Source 2 in the figure is only considered to be connected when initializing time-domain simulations. The test system was developed using the PSCAD software.

This test system was selected because the wind turbines and the series compensated network have an unstable interaction when the wind plant operates radially into the series compensated line. The interaction is primarily a control driven phenomena - the fast action of the rotor current control loop increases the rotor-side resistance, leading to negative resistance as seen from the stator. This is different but related to the traditional induction generator effect (IGE) due to the fast-acting nature of the Type 3 wind turbine controls

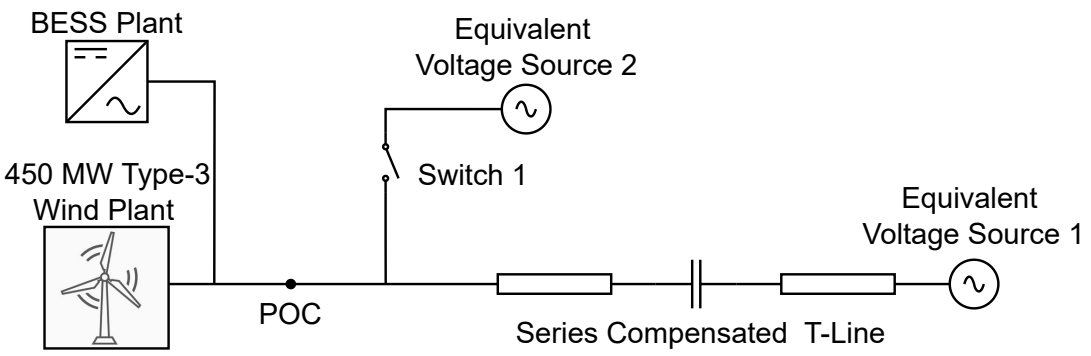

Figure 3.1: Test System Single-Line-Diagram

[33] [15]. The inductance of the wind turbine and the transmission system form a series resonance with the series capacitor, and if negative damping produced by the wind turbines overcomes the positive damping produced by the system at the resonant frequency, the interaction results in an unstable mode. This type of interaction has been observed a number of times in real world events [10], most famously in the South Texas event of 2009 [34], and continues to result in enforcement of expensive generation curtailment by system operators in present-day to avoid instabilities. Note that Type 3 wind plants are not the only types of IBRs which can become unstable due to a series system resonance, any device which is not purely passive at sub synchronous frequencies can become unstable if it provides negative damping to a network resonance. The type 3 wind plant is particularly prone to involvement in this sort of instability because of the induction generator effect resulting from the direct stator connection, which can lead to very poor damping characteristics across a wide range of sub-synchronous frequencies.

If the influence of the co-located BESS/wind plant is ignored, the resonant frequency of the radial network is primarily governed by the combined inductance of the transmission line and network equivalent, as well as the compensation level of the series capacitor, as described in Eq. (3.1). Consequently, higher levels of series compensation (i.e., reduced capacitance, C) and greater system strength (i.e., reduced inductance, L) both result in an increase in the system's resonant frequency.

$$\omega_{res} = \frac{1}{\sqrt{LC}} \tag{3.1}$$

3.2 Test System Details

The test system considered in this analysis consists of a grid-forming battery inverter connected in parallel with a 450 MW wind plant. The plant is connected into a 345 kV system through a long transmission line which contains a series capacitor at its midpoint. The series capacitor was configured to compensate the reactance of the transmission line at fixed levels of 25%, 50%, and 75% . The remote end of the transmission line is connected to an equivalent voltage source (Equivalent Voltage Source 1 in Figure 3.1), which has a short-circuit MVA ($SCMVA$) of 1350 MVA, and an X/R ratio of 10. A voltage source with the same parameters is also connected at the wind plant POC, however this is only used to initialize the time domain simulation. The transmission line is modeled as a frequency-dependent model. When the transmission line and a series capacitor with 50% compensation are considered, the resultant $SCMVA$ at the wind plant Point of Connection (POC) is approximately 1060 MVA with an X/R ratio of 8.6. The network equivalent on the remote end of the transmission line is relatively weak, which results in an Short Circuit Ratio (SCR) of 2 when the line is not series compensated and 2.35 when the line is 50% series compensated. This configuration was chosen to represent a transmission line which is loaded near the maximum practical power transfer limit, and would substantially benefit from series compensation. SCR is defined according to Eq. (3.2), where $SCMVA$ is the short-circuit current at the wind plant POC and MW_{WTG} is the wind plant rated power (450 MW). Parameters relevant to this calculation are provided in Table 3.1 below, in per-unit on 100 MVA base.

$$SCR = \frac{SCMVA}{MW_{WTG}} \tag{3.2}$$

Table 3.1: Test Grid Parameter Values

Description	Value (per-unit on 100 MVA, 345 kV base)
T-line R	0.0035
T-line X	0.039
T-line B	0.671
Series Capacitor Xc (50% comp.)	0.01805
System Equivalent R	0.0074
System Equivalent X	0.0741

Chapter 4

Impedance Scan Analysis

This section describes the impedance scan analysis used to verify the FDVI controller and to parameterize the FDVI controller. This was done by performing impedance scan analysis of the BESS and wind plant in isolation. The complete system model is investigated in Chapter 5.

4.1 Impedance Scan Methodology

The frequency-domain impedance of the BESS and the wind plant was determined using the DQ reference frame frequency scan methodology described in [35] and [36]. This method involves perturbing an ideal voltage source with voltages across a range of frequencies and then calculating the impedance (or admittance) based on the Fast Fourier Transform (FFT) of the device voltage and current at the connection point. Performing this scan in the DQ reference frame (as opposed to the sequence reference frame) is advantageous because inverters are commonly time invariant when modeled in the DQ under certain assumptions, but not necessarily in the phase/sequence frame, as described in [36]. Time invariance means

$$Y_{DQ}(jw) = \begin{bmatrix} \frac{\Delta I_D(j\omega)}{\Delta V_D(j\omega)} & \frac{\Delta I_D(j\omega)}{\Delta V_Q(j\omega)} \\ \frac{\Delta I_Q(j\omega)}{\Delta V_D(j\omega)} & \frac{\Delta I_Q(j\omega)}{\Delta V_Q(j\omega)} \end{bmatrix} \tag{4.1}$$

that the state-space model of the inverter can be expressed without any time-dependent terms in the state-space matrices. The property of time invariance is necessary to frequency scanning because frequency-domain transfer functions are not valid for time varying systems. Time invariance also entails that when a signal of a certain frequency is injected into the system, it elicits a response only at that frequency and no other complementary frequencies. This is explained in detail in [37].

Scanning a device in the DQ frame involves perturbing the D-axis and Q-axis voltages separately in order to calculate all elements in the DQ domain 2x2 admittance matrix $Y_{DQ}(jw)$, as shown in in Eq. (4.1). One can calculate the impedance across a range of frequencies by injecting a perturbation signal which contains a multitude of frequency components (multi-sin signal), or one frequency can be scanned at a time. In this process, care was taken to ensure that the magnitude of the perturbation signal only triggers the small-signal response of the device being scanned, without triggering non-linear modes of operation. The DQ reference frame admittance can be transformed to the sequence reference frame admittance ($Y_{PN}(jw)$ and vice-versa following the process shown in Figure 2 of [35].

4.2 Wind Plant Impedance Scan

The positive-sequence impedance of the type-3 wind plant in the medium wind generation scenario is shown in Figure 4.1. The resistance of the wind plant considered in this analysis is negative starting at 5 Hz, indicating that the plant will be prone to unstable interaction with system series resonances occurring across a wide range of sub-synchronous frequencies because the magnitude of negative resistance will be greater than any positive resistance offered by the grid impedance. Note that the model used in this analysis is a generic representation that was not specifically designed or tuned for operation in a series-compensated network. Consequently, it represents a conservative case compared to modern Type-3 WTGs,

which typically include control enhancements, such as damping controllers, to improve performance in this frequency range. These enhancements have been implemented over the years in response to the well-known challenge of W-SSCI.

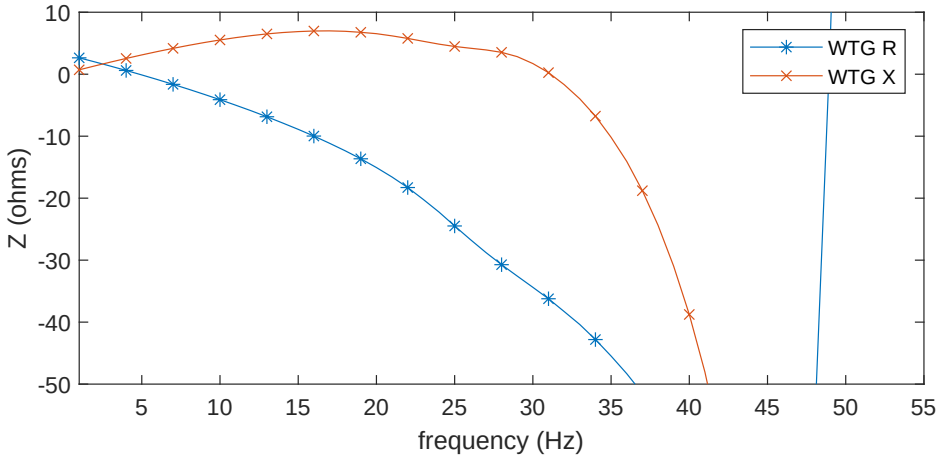

Figure 4.1: Positive Sequence Impedance of Wind Plant

4.3 FDVI Verification

The FDVI controller was verified by applying a virtual resistance of 0.05 pu at 30 Hz in the grid-forming BESS and comparing the positive-sequence impedance to the unmodified grid-forming BESS. A virtual reactance of 0.05 pu at 30 Hz was also applied and tested. These scans are shown in Figure 4.2. It can be seen that the virtual resistance appears at the expected frequency and magnitude, and that there is some cross-coupling impact on the reactance as well due to the complex nature of the band-pass-filter transfer function. For the grid-following BESS, the FDVA controller was verified in a similar way.

4.4 Grid-Forming FDVI Parametrization Process

The center frequency of the BPFs and values of virtual resistance / reactance in the grid-forming inverter's FDVI controller were determined through an optimization process which

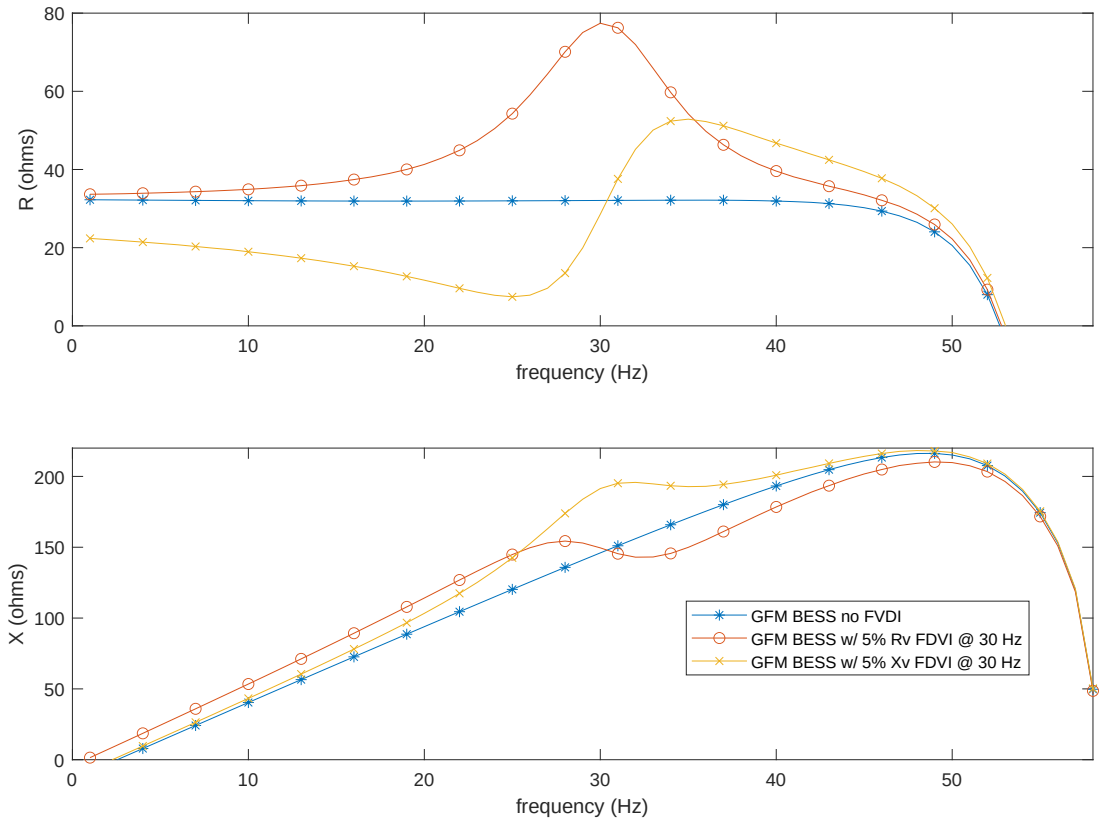

Figure 4.2: Positive Sequence Impedance Verification of FDVI Controller

had the objective of using the admittance of the BESS to make the combined BESS plus wind plant admittance appear passive (i.e. positive conductance) to the network over the critical frequency range. If the conductance of the combined plant is positive, the system will be passive and will therefore be stable. The concept of passivity concept can be expanded to more complex systems involving many more devices, as discussed in [38]. A Genetic Algorithm numerical optimization method was used for this parametrization because the analytical relationship between the conductance characteristic and the parameters of the FDVI loop was found challenging to realize. The details of the optimization method are explained later in this chapter.

The optimization process aims to minimize the total negative conductance resulting from the combined behavior of the grid-forming inverter, $G_{GFM}(s)$, and the wind plant, $G_{WTG}(s)$. To achieve this, the magnitude of virtual resistance and reactance, as well as the center

frequencies of the associated band-pass filters, were adjusted to shape the overall conductance profile. A more straightforward approach would involve directly modifying the conductance shape of the inverter using a virtual admittance controller, however this method did not yield the anticipated results. The exact cause remains unclear, but it is likely linked to the influence of the current feed-forward terms in the inner voltage control loop.

An impedance scan analysis approach in the PSCAD simulator was used to perform the optimization, following a similar approach described in [35]. Figure 4.3 describes the optimization process. In this process, the positive-sequence admittance was calculated based on positive-sequence voltage injection, instead of the DQ method described in Section 4.1. Scanning for admittance in the sequence reference frame for the optimization is computationally efficient, which was important due to the relatively slow simulation speed in the PSCAD simulator, but is not as accurate as scanning in the DQ reference frame. However, for this case, a comparison of the resulting admittance difference between DQ and sequence reference frame was performed and was not substantial in the frequency range of interest.

Using only the positive sequence component of admittance ignores the effect of the positive-negative sequence cross-coupling components of $Y_{DQ}(jw)$, which was acceptable in this case because these components were relatively small in the frequency range of interest. The negative sequence component of $Y_{DQ}(jw)$ was also ignored for computational efficiency, but could have been incorporated to make the process more complete.

The positive-sequence admittance of the wind plant ($G_{WTG\,AVG}(s)$) was determined external to the optimization loop. Because the admittance of the wind plant was found to change significantly depending on the operating point, the admittance used in the optimization process is the average admittance of the wind plant across a low, medium, and high wind scenario. Since the wind plant and BESS plant are connected at the same point, the total admittance can be found by simply summing the admittance of the two devices together in the frequency-domain. The BESS was assumed to be rated at 200 MW (44% of the wind plant rating) for the purposes of the parameter optimization, however the rating of the BESS

was changed as part of the analysis in following chapters. The sum of the total negative admittance from 5 to 45 Hz formed one component of the objective function, as shown in Eq. (4.2).

Optimizing the BESS solely based on its admittance characteristics is not recommended, as doing so may result in significant transient performance issues due to the influence of the

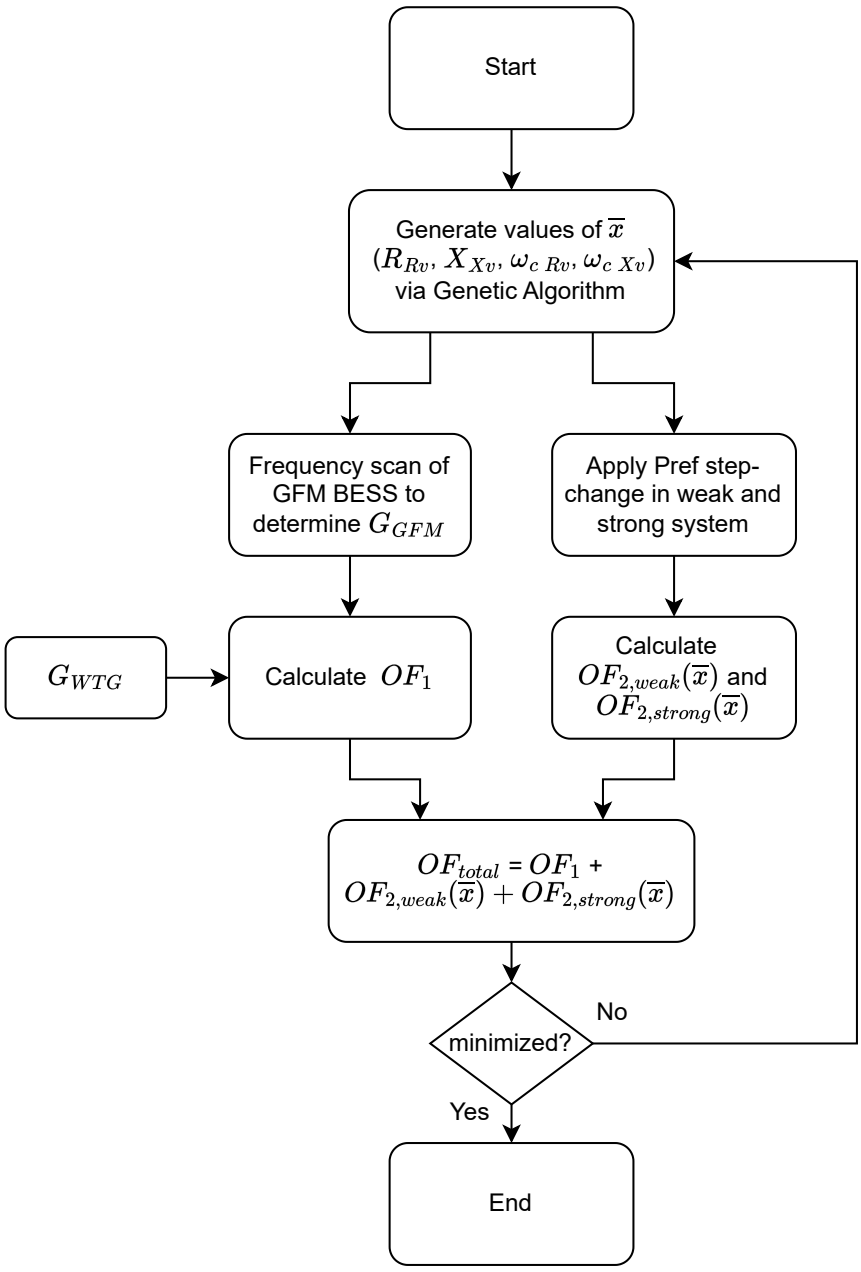

Figure 4.3: Optimization Process to Determine Virtual Resistance / Reactance Parameters

$$OF_1(\overline{x}) = \sum_{\omega=2\pi5}^{2\pi45} W_1(s)|G_{GFM}(s,\overline{x}) + G_{WTG\,AVG}(s)| \tag{4.2}$$

$$OF_2(\overline{x}) = \int_0^{T_s} \left(P_{BESS}^{\text{ref}}(t) - P_{BESS}(t,\overline{x})\right)^2 dt \tag{4.3}$$

$$OF_{total}(\overline{x}) = OF_1(\overline{x}) + OF_{2,weak}(\overline{x}) + OF_{2,strong}(\overline{x}) \tag{4.4}$$

FDVI. To account for this, a second objective function was introduced which calculates the cumulative time-sequence error in active power when a step-change in active power reference is given to the BESS. This check was applied in a weak system and a strong system to account for the potential stability sensitivity to system strength. This second objective function is shown in Eq. (4.3), and the total objective function in Eq. (4.4). The weighting function $W_1(s)$ in Eq. (4.2) was configured to heavily weigh the frequency range from 5 to 35 Hz and then decay from 36 Hz to 45 Hz, because it is less likely to encounter W-SSCI at higher frequencies. $W_1(s)$ was also used to weigh the total objective function towards OF_1 so that changes in the total conductance are favored over changes in dynamic stability.

Multiple optimization methods were tried, including Simplex [39] and Genetic Algorithm [40]. Despite having only four parameters to optimize, Simplex repeatedly settled to local minima, so the Genetic Algorithm optimization was used in the final optimization. The Genetic Algorithm was configured with an initial population of 100, surviving generation of 80, mating pool population of 40, elite population of 10, and a 5% mutation rate.

The proposed parameter optimization method outlined above focuses on enforcing passivity of the combined BESS and wind plant over a specific frequency range, which does not require any grid information. Additionally, it does not require specific control implementation details from the co-located wind plant, which may be considered intellectual property. Therefor, this method could be used by plant developers to tune control loops of co-located BESS inverter to provide damping in series-compensated system, with the only input required being the conductance curve of the wind plant.

4.5 BESS Parameter Optimization Results

4.5.1 Grid-Forming FDVI Optimization Results

In order to minimize the negative conductance of the wind plant, the conductance of the BESS needs to be maximized. Since the conductance is impacted by both the resistance and reactance, the optimization function included both a virtual resistance and a virtual reactance term. Comparisons of the resulting conductance of the wind plant by itself, and the wind plant in parallel with the grid-forming BESS (with and without optimized FDVI) are shown in Figure 4.4. The introduction of the grid-forming BESS reduces the frequency range of negative conductance of the combined system due to the natural large positive conductance of the grid-forming BESS, and the addition of the optimized FDVI provides even more positive conductance. The optimal virtual impedance parameters are shown in Table 2.1. Adding the grid-forming BESS without virtual impedance reduced the objective function from 1.64 to 0.89, and adding the FDVI with the optimized parameters further reduces the objective function to 0.55.

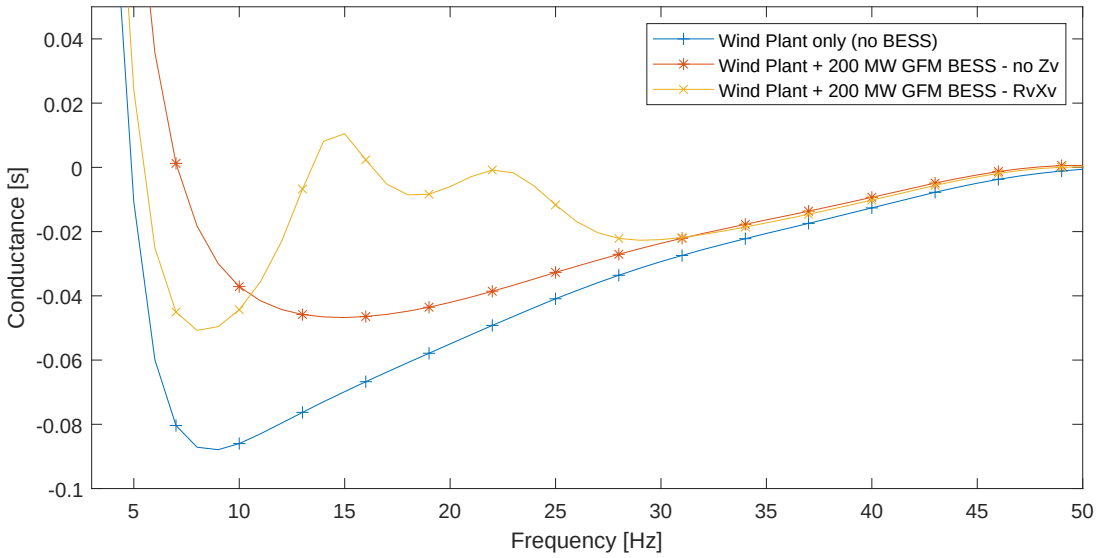

Figure 4.4: Comparison of Positive Sequence Conductance of only Wind Plant, and Wind Plant in parallel with 200 MW Grid-Forming BESS (With and Without FDVI)

4.5.2 Grid-Following FDVA Optimization Results

The parametrization of the FDVA controller in the grid-following BESS model was optimized following the same process described for the grid-forming FDVI loop in Figure 4.3, however only virtual conductance was considered for the grid-following BESS to limit complexity and because virtual susceptance would only impact the conductance via the cross-coupling effect observed in Figure 4.1. Comparisons of the resulting conductance of the wind plant by itself, wind plant in parallel with grid-following BESS (with and without FDVA) are shown in Figure 4.5.

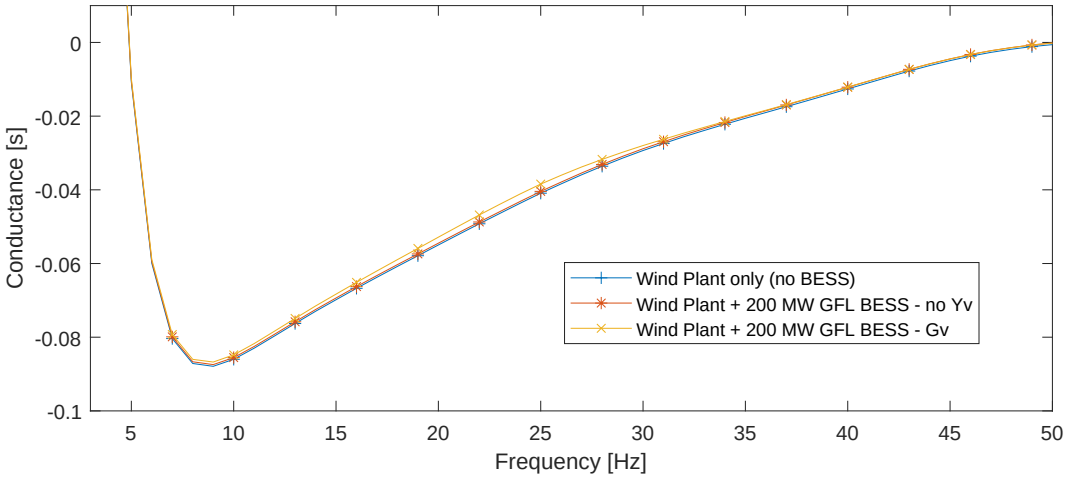

Figure 4.5: Comparison of Positive Sequence Conductance of only Wind Plant, and Wind Plant in Parallel with 200 MW Grid-Following BESS (With and Without FDVA)

The 200 MW grid-following BESS was not able to substantially shift the conductance of the wind plant even with the optimized FDVA controller. This is because the grid-following BESS naturally has a much lower admittance than the grid-forming BESS. Figure 4.6 shows the comparison of the grid-following conductance, grid-forming conductance, and the wind plant conductance. Because of the inherently low admittance, the FDVA controller of the grid-following BESS would require very large gains to significantly influence the wind plant. However, time-domain tests showed that such large gains are prohibitive as they destabilize the grid-following BESS. The optimized FDVA parameters are provided in Table 2.3.

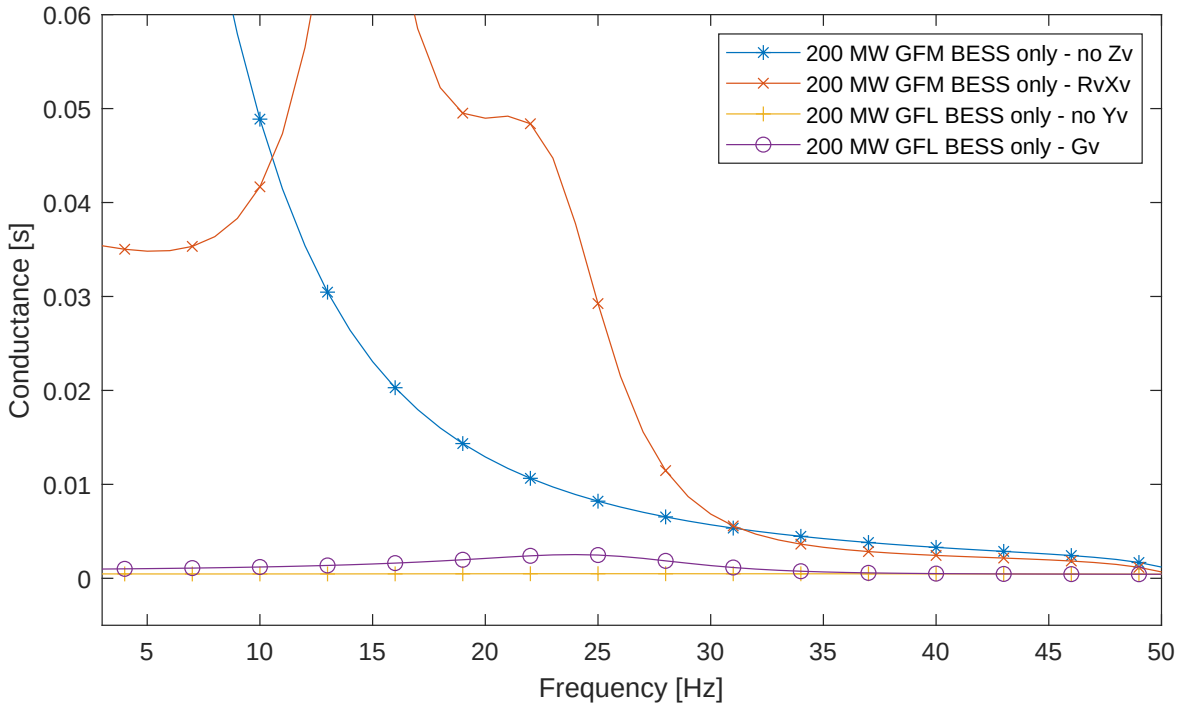

Figure 4.6: Comparison of Positive Sequence Conductance of Grid-Forming BESS and Grid-Following BESS

Chapter 5

Full System Analysis

The full test system was analyzed using eigenvalue analysis in MATLAB and time-domain simulations in PSCAD to determine the minimum BESS rating required for system stabilization. The BESS was evaluated in various configurations, including grid-forming with and without the FDVI controller, as well as grid-following with and without the FDVA controller. Series compensation levels were tested at 25%, 50%, and 75%, while wind generation scenarios were assessed at low (30%), medium (50%), and high (100%) levels. To manage complexity, the analysis was limited to these specific cases. Consequently, intermediate conditions that might yield more favorable or less favorable stability outcomes were not examined. When the rating of the BESS is changed in this analysis, the full BESS plant is scaled up or down. This means the absolute ratings of the BESS electrical elements (transformer, LCL filter), as well as the BESS inverter current limits, change in proportion to the scaling factor.

5.1 Eigenvalue Analysis

The full test system was first analyzed using an eigenvalue-based approach. The eigenvalue approach, despite its complexity, was chosen over other stability assessment methods, such as advanced impedance-based techniques [41] [42], due to its comprehensive nature and

because we can clearly track trajectory of the various modes involved. This approach involves obtaining the state-space model of individual parts of the system, combining all the parts into a single state-space matrix, and then extracting the eigenvalues. The state-space models of the BESS and wind plant were obtained by performing a DQ reference frame frequency scan analysis in PSCAD in order to extract the frequency-domain DQ admittance $Y_{DQ}(s)$ of each device, as outlined in Section 4.1. The frequency scan was performed one time for a specific rating of BESS, which could then be easily modified to represent a BESS plant of a different rating by applying a scaling factor to the BESS DQ admittance curves. This allows for analysis of many different rating values without re-performing the frequency scan, which is a time-consuming process.

The resultant DQ admittance curves were vector-fit [43] to obtain the state-space representation of the BESS (A_{BESS}, B_{BESS}, C_{BESS}, D_{BESS}) and wind plant (A_{WTG}, B_{WTG}, C_{WTG}, D_{WTG}). Care was taken to select an appropriate order of fit for each model. The state-space model of the BESS in parallel with the wind plant was found according to Eq. (5.1). DQ impedance curves of the series-compensated network were obtained through network reduction methods available in the PSCAD program. These were also curve-fit to determine the network state-space model (A_G, B_G, C_G, D_G). The combined system state-space model A_T was then calculated as shown in Eq. (5.2). The system considered in the Eigenvalue analysis is the radial system, with Voltage Source 2 from Figure 3.1 disconnected.

$$A_P = \begin{bmatrix} A_{BESS} & 0 \\ 0 & A_{WTG} \end{bmatrix} \quad , \quad B_P = \begin{bmatrix} B_{BESS} \\ B_{WTG} \end{bmatrix}$$
$$C_P = \begin{bmatrix} C_{BESS} & C_{WTG} \end{bmatrix} \quad , \quad D_P = \begin{bmatrix} D_{BESS} + D_{WTG} \end{bmatrix} \tag{5.1}$$

$$A_t = \begin{bmatrix} A_G - B_G N D_P C_G & -B_G N C_P \\ B_P M C_G & A_P - B_P M D_G C_P \end{bmatrix}$$
$$N = (I + D_P D_G)^{-1} \tag{5.2}$$
$$M = (I + D_G D_P)^{-1}$$

5.1.1 Stage-Space Model Development Discussion

The method used to obtain the state-space model of the full system described above does not involve deriving analytical models of the various devices, relying rather on frequency scanning and curve fitting techniques. The primary advantage of the frequency scanning method is that it allows for the characterization of arbitrarily complex black-boxed models, while the analytical method requires full insight into the structure and parameterization of all relevant control loops. This level of information is not disclosed by inverter vendors to external model users in most cases due to intellectual property concerns, leaving frequency scanning as the only option in many real-world study scenarios. However, there are a number of possible sources of inaccuracy in the frequency scanning and curve fitting process, particularly related to inappropriate choice of perturbation magnitude, number of frequencies to perturb simultaneously, curve-fitting parameters, and improper filtering of input data. These were accounted for by performing various sensitivities and validations, and the end result was ultimately verified by time-domain testing.

5.1.2 Eigenvalue Analysis without BESS

First, an analysis of the system without the BESS was performed. The wind plant was tested at three different generation levels, with three different levels of series compensation. The resulting eigenvalues are shown in Figure 5.1.

The eigenvalue analysis identifies two primary modes of interest, with the W-SSCI mode occurring between 25 and 45 Hz. Table 5.1 presents the frequency and damping ratio of

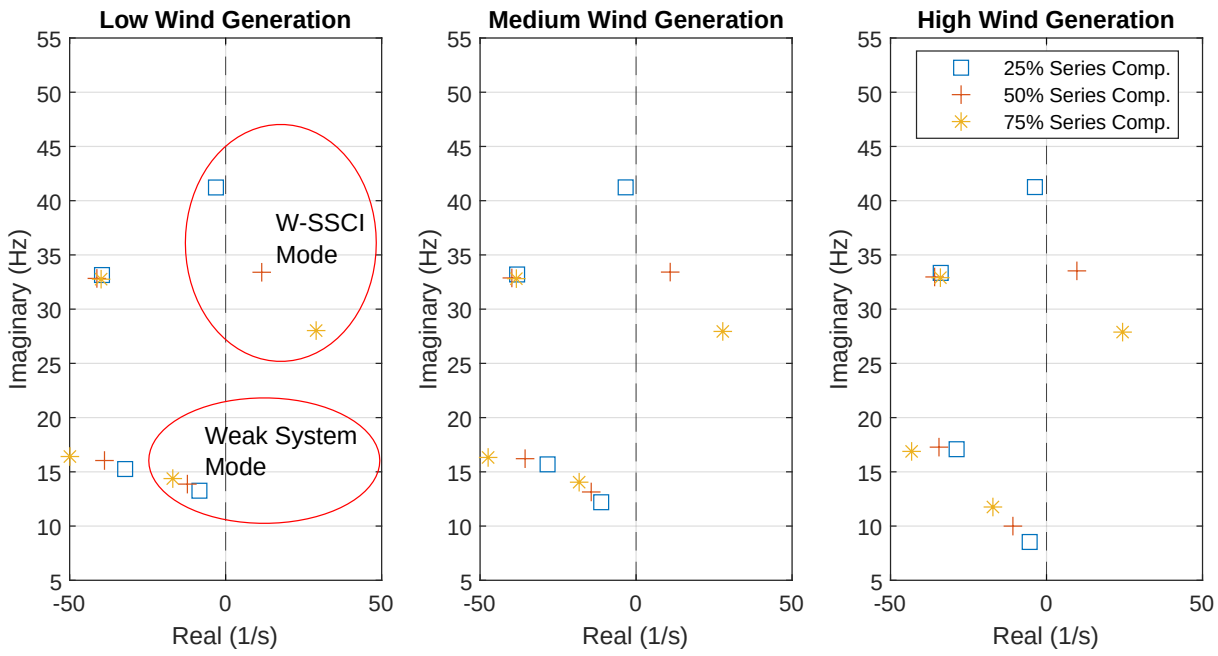

Figure 5.1: Eigenvalues of the Test System Before Addition of BESS

the W-SSCI mode under various conditions. The damping and frequency of this mode are highly influenced by the series compensation level: The 25% compensation scenario remains stable, while the 75% scenario is highly unstable across all levels of wind generation. Higher series compensation levels result in a more unstable W-SSCI mode due to their effect on the system's series resonance frequency.

In the sequence frame of reference, increasing compensation level also increases the resonance frequency, which, as shown in Figure 4.1, amplifies the negative resistance behavior of Type-3 wind plants at higher frequencies which further destabilizing the system. Additionally, Table 5.1 highlights that wind generation levels also affect the W-SSCI mode. For the 75% compensation scenario, the damping ratio worsens from -13.8% at high wind generation to -16.3% at low wind generation. This variation arises because the wind plant's operating conditions influence its impedance, leading to reduced damping at lower generation levels. The W-SSCI mode also shows significant sensitivity to the rotor-side current control gains. By reducing the proportional and integral gains (K_p and K_i) of the current control loop by

50%, the eigenvalues, plotted in Figure 5.2, indicate a substantial improvement in stability across all levels of wind generation.

Wind Level	Series Comp. Level	Frequency (Hz)	Damping Ratio (%)
Low Wind	25%	41.2	1.2%
	50%	33.4	-5.5%
	75%	28.0	-16.3%
Mid Wind	25%	41.2	1.3%
	50%	33.4	-5.2%
	75%	27.8	-15.8%
High Wind	25%	41.3	1.4%
	50%	33.5	-4.6%
	75%	27.9	-13.8%

Table 5.1: W-SSCI mode details for Different Wind and Series Compensation Levels

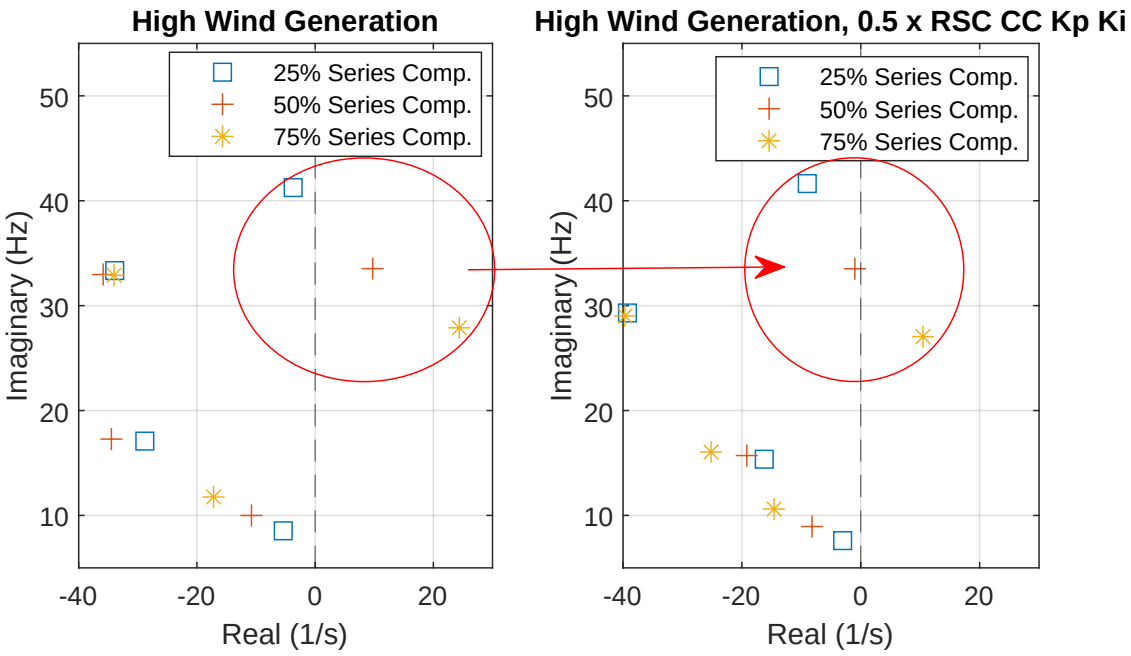

Figure 5.2: Eigenvalues Before and After Reducing WTG Rotor-Side Converter Current Controller Gains

The mode occurring between 5 and 15 Hz exhibits significant sensitivity to the effective system impedance and the gains of the wind plant's AC voltage controller (within the Q-axis of the rotor-side controller). Figure 5.3 illustrates the eigenvalues for the high wind

scenario with default controller gains, compared to a sensitivity case where the proportional gain of the AC voltage controller was doubled. This increase in gain shifts the mode to the unstable region of the eigenvalue plot across all three compensation levels, demonstrating strong sensitivity. Higher series compensation levels reduce grid impedance, which stabilizes this mode, whereas increased wind plant generation levels raise power transfer through the network, leading to destabilization. With the default voltage controller gains, this mode remains stable in all scenarios. Due to its pronounced sensitivity to voltage control gains, system impedance, and active power transfer, this mode is referred to as the "weak system mode" throughout the remainder of the thesis.

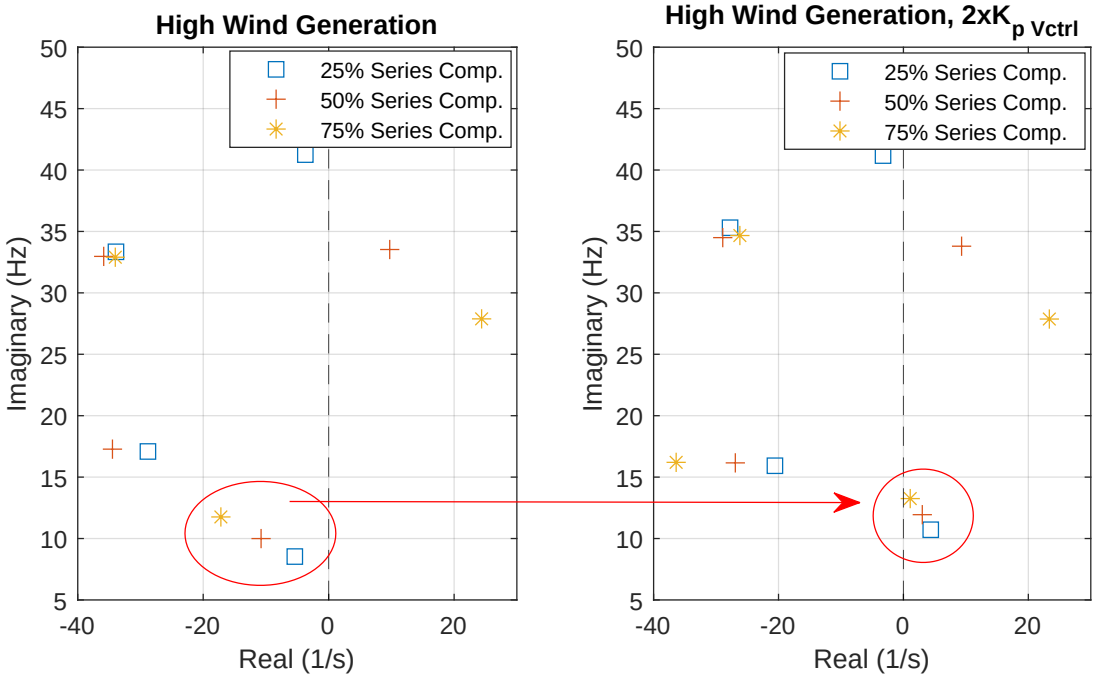

Figure 5.3: Eigenvalues Before and After Increasing WTG Voltage Control Gain

5.1.3 Eigenvalue Analysis with BESS

The impact of the BESS on the series compensated system was assessed by scaling up the MW rating of the BESS until the system is marginally stable. The BESS was tested in

Wind	Series Comp.	BESS marginally stable power rating (% of wind plant rating)			
		GFM, no FDVI	GFM, FDVI	GFL, no FDVA	GFL, FDVA
Low	50%	33%	19%	none found	444%
	75%	51%	38%	none found	944%
Med.	50%	32%	18%	none found	none found
	75%	51%	36%	none found	none found
High	50%	30%	18%	none found	none found
	75%	49%	36%	none found	none found

Table 5.2: Minimum BESS Rating Needed to Stabilize Unstable Modes in Eigenvalue Analysis, Expressed as % of Wind Plant Rating

grid-forming and grid-following configurations, with and without the frequency-dependent impedance / admittance controllers. The rating of the BESS is expressed as a percentage of the rating of the wind plant.

Figure 5.4 shows the locus of the sub-synchronous eigenvalues as the MW rating of the grid-forming-configured BESS is increased from 0 MW to 66% of the wind plant rating (300 MW) for all three wind scenarios, and for all three series compensation levels. The figure includes plots with the grid-forming BESS configured with the FDVI controller (RvXv) and without (no Zv). In the most severe case (75% series compensation, Low Wind), the grid-forming BESS was able to stabilize the system when rated at 51% (230 MW) without FDVI, and 38% (170 MW) with FDVI. In the more moderate 50% series compensation case, a BESS rating as small as 19% (85 MW) was found to stabilize the W-SSCI when FDVI was enabled. The ratings of the grid-forming BESS at which the W-SSCI mode crosses from unstable to stable for all cases are reported in Table 5.2. It can also be seen that the weak system mode (occurring at 10-15 Hz) becomes increasingly well damped as the rating of the grid-forming BESS is increased, even with very small BESS ratings. Additionally, the new modes introduced by the FDVI controller are visible in the eigenvalue plots, occurring between 35 Hz and 50 Hz. These modes are reasonably well damped and appear to be starting to move in the stable direction at the 66% (300 MW) rating.

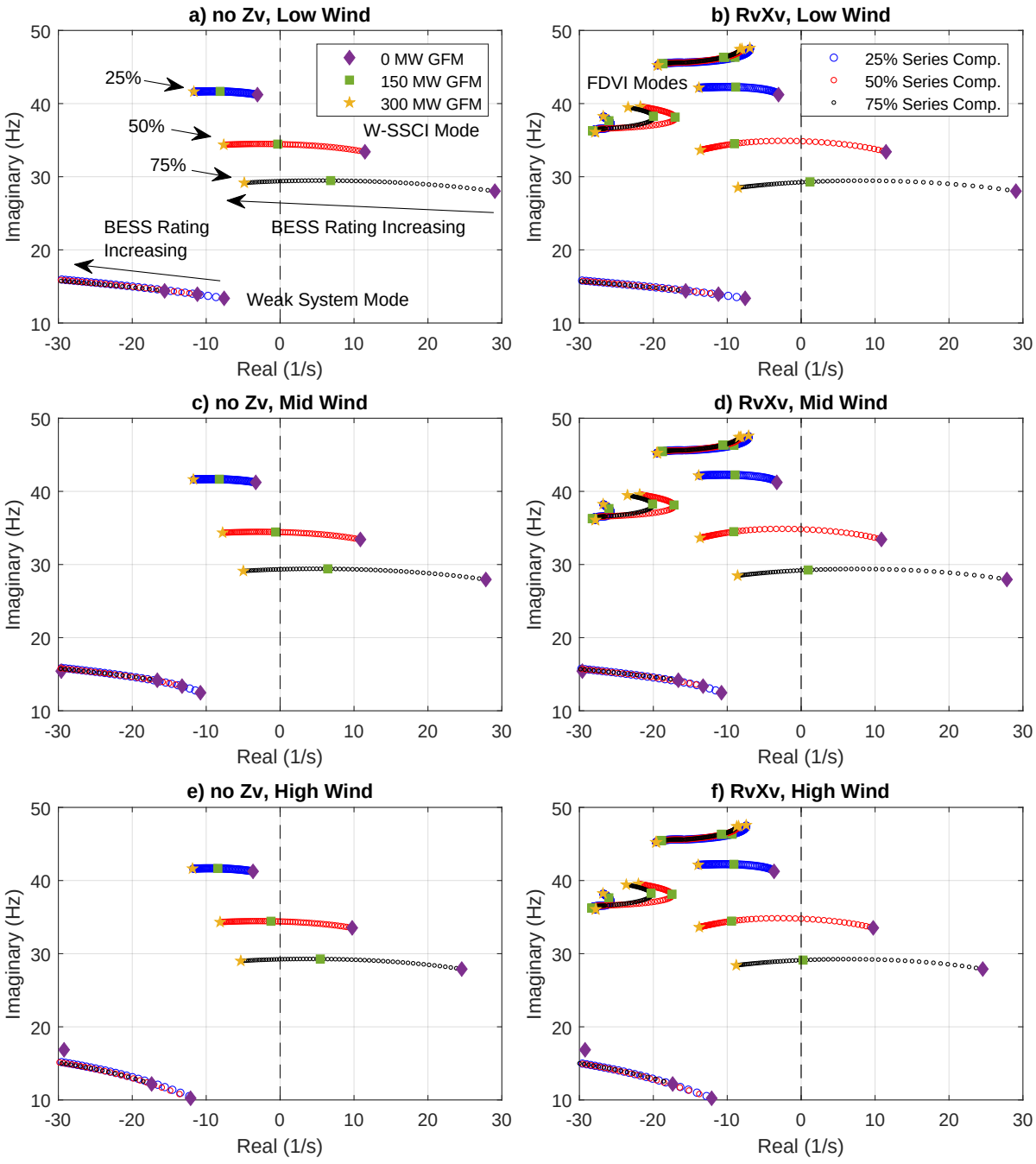

Figure 5.4: Locus of Critical Eigenvalues of the System when Rating of Grid-Forming BESS is Increased from 0 to 300 MW With Grid-Forming BESS Configured Without FDVI (no Zv) and With FDVI (RvXv), Tested for All Wind Generation and Series Compensation Levels

When the BESS is configured as grid-following, the marginally stable points occur at much higher BESS ratings, and in some cases, a stable condition is not achievable. Figure 5.5 shows the locus of sub-synchronous eigenvalues as the MW rating of the grid-following BESS is increased from 0 MW to 1100% of rating of the wind plant (5000 MW) across all wind generation and series compensation scenarios. Without FDVA, the W-SSCI mode shows minimal movement, and even a 5000 MW BESS does not stabilize any of the 50% or 75% series compensation cases. This is due to the characteristically low admittance of the unmodified grid-following BESS. However, when FDVA is enabled, the W-SSCI mode eventually stabilizes for a very large BESS rating. Specifically, a 944% (4250 MW) BESS is required to stabilize the 75% series compensation / low wind case.

When the BESS was configured as grid-forming, the weak system mode was stabilized with a small BESS rating and became more stable as the BESS rating was increased. In contrast, when the BESS is configured as grid-following, the weak system mode became less stable as the BESS rating increased. In many instances, the weak system mode destabilized before the W-SSCI mode stabilized, meaning that the system could not be stabilized with any rating of BESS (as indicated by the 'none found' entries in Table 5.2). Additionally, the presence of the FDVA controller accelerates the destabilization of the weak system mode. In the worst-case weak system scenario (high wind, 25% series compensation), the grid-following BESS with FDVA destabilizes the weak system mode at a 56% (250 MW) rating, compared to 78% (350 MW) without FDVA.

Due to the extreme BESS capacity required to stabilize the W-SSCI mode, along with the exacerbation of the weak system mode, the grid-forming BESS offers a clear advantage over the grid-following BESS for this application. It should be noted that control modifications, such as implementing fast inverter-level voltage and frequency control, could significantly increase the admittance of the traditionally-controlled grid-following inverter. However, it could be argued that there is limited benefit in modifying grid-following BESS inverters to resemble grid-forming inverters when grid-forming BESS inverters are already commercially

available.

The significant difference in the minimum BESS ratings required to stabilize the system when configured as grid-forming versus grid-following can largely be attributed to the inherent admittance differences between these devices. The grid-forming inverter behaves like a voltage source with low impedance (small admittance), while the grid-following inverter behaves as a current source in parallel with high impedance, or as a voltage source behind a large impedance (small admittance). Therefore, the results from the grid-following benchmark are not wholly unexpected.

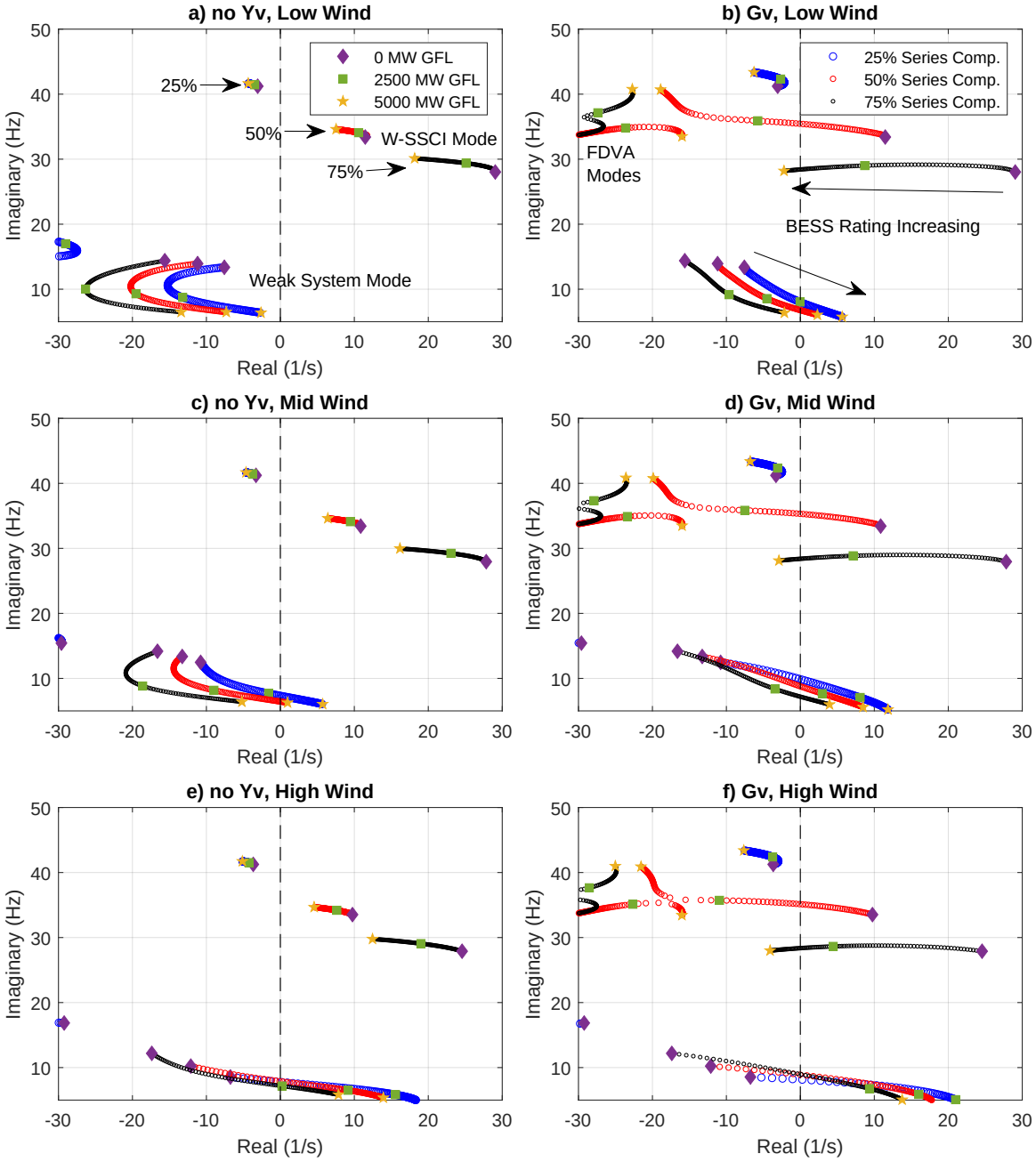

Figure 5.5: Locus of Critical Eigenvalues of the System when Rating of Grid-Following BESS is Increased from 0 to 5000 MW With Grid-Forming BESS Configured Without FDVA (no Yv) and With FDVA (Gv), Tested for All Wind Generation and Series Compensation Levels

5.2 EMT Time-Domain Analysis

An EMT time-domain analysis was performed using EMTDC/PSCAD to verify the results of the eigenvalue analysis, as well as investigate potential large-signal impacts. The test system is initially configured with Switch 1 from Figure 3.1 closed, which allows the system to find a stable initial operating condition. At 5 s after the start of the simulation, a fault is applied at at the Equivalent Voltage Source 2, and at 5.1 s Switch 1 is opened to clear the fault. The resultant system has a radial path between the wind plant / BESS and the series capacitor, which is the same system analyzed in the eigenvalue analysis. The change in network topology also creates a change in the system voltage phase angle.

5.2.1 Grid-Forming BESS Time-Domain Simulation

Figure 5.6 shows plots of several POC measurements for the fault and line outage when the BESS is grid-forming-configured and is rated to 28% of the wind plant (125 MW), with and without FDVI. A 50% compensation level and a medium wind generation level was assumed. The behavior during the fault is nearly identical, however short after fault clearing there is a clear difference in damping. The grid-forming BESS without FDVI is not able to damp the W-SSCI mode, with voltage oscillations quickly growing to 5% within 0.7 s of fault clearing. When the grid-forming BESS has the FDVI controller enabled, the W-SSCI mode is well damped within the 0.7 s following the switching event. This result is in-line with the eigenvalue analysis reported in Table 5.2, which predicts that the grid-forming BESS with FDVI is stable when rated to at least 80 MW, and that without FDVI the BESS will be unstable if rated less than 145 MW. The frequency of oscillation and damping factor were approximated from the time-domain simulation based on logarithmic decrement. When compared to the eigenvalue analysis, the frequency of oscillation compared to within 0.1 Hz, and the damping factor to within 0.01%, which indicates a very good match. This was true for the case with and without FDVI enabled.

The inherent grid-forming voltage-source response is also demonstrated in these time-domain simulation results. During the fault, the grid-forming plant immediately responds by injecting some active current and significant levels of reactive current into the grid. At fault clearing there is a large active power response to the the phase-angle change in the system. These responses are not due to dedicated LVRT controllers, but rather due to the constant voltage phasor maintained at the grid-forming inverter terminals. Due to the near overlap of the results with and without the FDVI controller in this period, we can conclude that the FDVI controller does not inhibit or decrease the voltage-source characteristic of the grid-forming inverter for this event.

5.2.2 Grid-Following BESS Time-Domain Simulation

The same event was simulated with the BESS configured as grid-following and rated to 555% of the wind plant (2500 MW). The simulation plots for this case are shown in Figure 5.7. The grid-following BESS without FDVA is not able to provide any significant damping benefit, leading to the wind plant becoming very unstable and tripping offline within 0.3 s. When FDVA was enabled, the W-SSCI mode is stabilized within about 0.5 s; however, the 8 Hz weak system mode is slowly growing. The frequency of oscillation and damping ratio of the W-SSCI mode in the time-domain simulation was approximated and compared to the eigenvalue analysis. With and without FDVA enabled, the frequency of oscillation compared to within 0.8 Hz, and the damping factor within 0.5%. These differences are likely a result of the grid-following BESS inverter either triggering various non-linear controllers in the wind plant or substantially changing the operating point of the system due to its very large rating compared to the capacity of the system and wind plant, both of which can result in changes to the oscillatory modes of the system. Additionally, there may be inaccuracies in use of the logarithmic decrement method to determine damping factor due to presence of multiple oscillatory modes. Despite these differences, the time-domain and eigenvalue analysis results are still generally in agreement, and the study conclusions do not change.

During the fault, the grid-following inverters don't output substantial amounts active or reactive current because there are no LVRT controllers included, however there is an oscillation present in the reactive output that is more severe when FDVA is enabled, leading to larger voltage fluctuations during the fault and at fault clearing. This result suggests that there is a trade-off between the damping provided and the transient performance for the grid-following inverter, which does not appear to be the case for the grid-forming inverter in this situation.

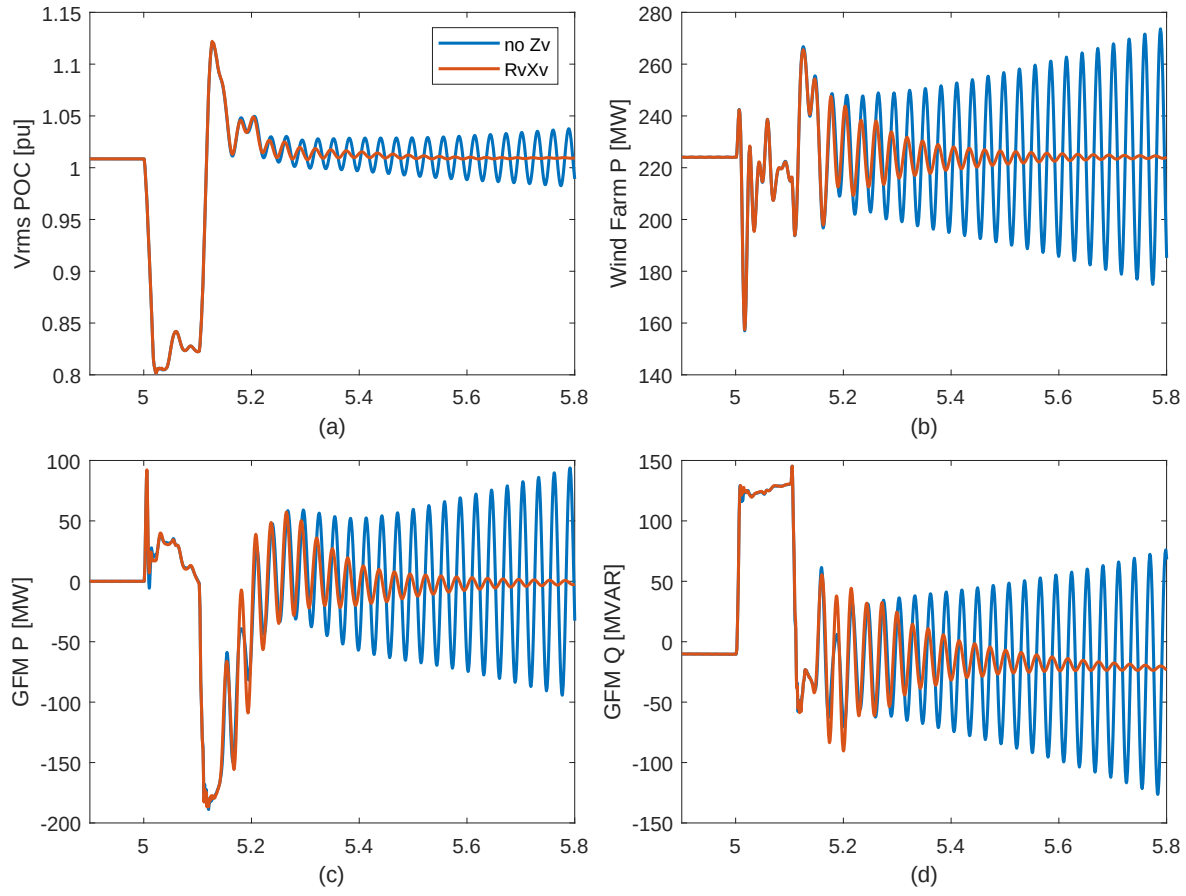

Figure 5.6: Plots of PSCAD Simulation Results at the Wind Plant POC in Response to the Fault Event with Grid-Forming BESS Configured With and Without the FDVI Controller, and Rated to 125 MW. 50% Series Compensation, Medium Wind Scenario.

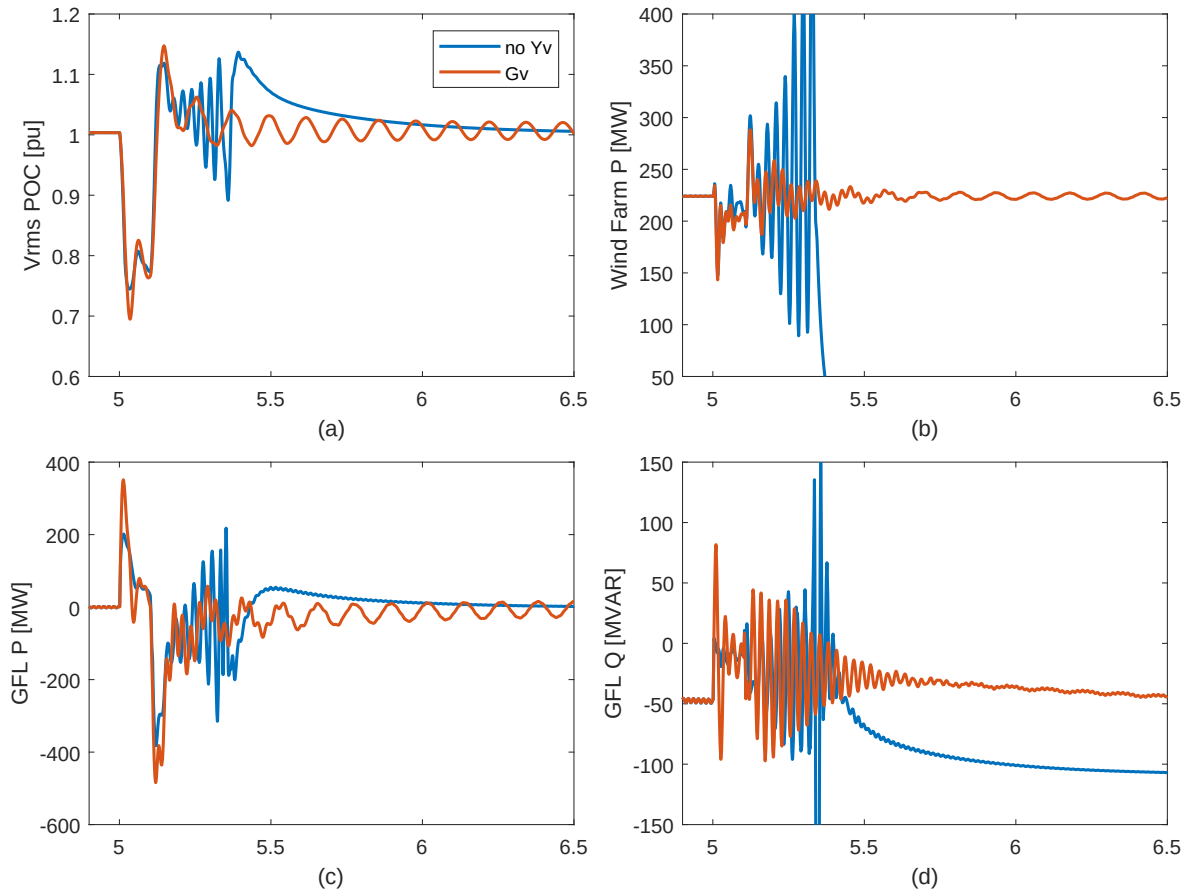

Figure 5.7: Plots of PSCAD Simulation Results at the Wind Plant POC in Response to the Fault Event with Grid-Following BESS Configured With and Without the FDVA Controller, and Rated to 2500 MW. 50% Series Compensation, Medium Wind Scenario.

Chapter 6

Conclusions and Future Work

This thesis investigated grid-forming technology in battery inverters as a mitigation to sub-synchronous oscillations (W-SSCI) between series-compensated systems and wind plants using Type-3 turbines. A new frequency-dependent virtual-impedance method was proposed in order to further elevate the performance of the grid-forming inverters. A comparative analysis of grid-forming and grid-following inverters was performed to provide a performance benchmark. To do this, models of the inverters and the series-compensated test system were first developed in PSCAD. Next, an impedance scan approach was used to parameterize certain inverter control loops and to gain understanding of the sub-synchronous behavior of the inverters. Finally, the full test system, including battery inverters, wind plant, and series compensated network was analyzed in an eigenvalue analysis and time-domain simulations. The conclusions of this study, as well as potential future work ideas, are presented below.

6.1 Conclusions

The overall research objective of investigating grid-forming damping behavior in the presence of W-SSCI and testing the proposed FDVI controller was achieved. Throughout this work, the following conclusions were drawn in support of this objective.

6.1.1 Grid-Forming BESS Performance

Through the impedance scan analysis and the eigenvalue analysis, it was found that the grid-forming BESS inverter was able to provide strong levels of damping to the W-SSCI-prone test system. With the research models used in this analysis, the grid-forming BESS inverter rated to 150 MW without modification was able to marginally damp the W-SSCI of a 450 MW wind plant in the moderate 50% series compensation scenario, and a 230 MW BESS was needed in the more severe 75% series compensation scenario. This was primarily due to the relatively high admittance characteristic, and more specifically the conductance characteristic, of the grid-forming inverter in the sub-synchronous frequency range. This high conductance is able to off-set the negative conductance introduced by the Type-3 wind plant, which allows for the overall resistance of the system at the resonant frequency to become positive. An added advantage of the grid-forming inverter was that the weak-system mode present in this test system, which was modestly damped in some scenarios, is well damped by even a very small BESS.

The benefit of the FDVI controller was exemplified through the reduced BESS rating needed to provide stability. In the eigenvalue study, it was found that the minimum BESS rating could be reduced by 25% to 45%, depending on the study scenario, when the FDVI controller was enabled. The primary benefit that the FDVI controller provided was that the conductance of the grid-forming inverter in critical frequency ranges can be substantially increased without compromising the overall stability of the inverter. These results verified that the impedance scan based optimization technique presented in Chapter 4 was successful in parameterizing the FDVI loop for improved performance.

6.1.2 Grid-Following BESS Performance

The performance of a grid-following BESS inverter was provided as a benchmark to the grid-forming. The analysis showed that the grid-following BESS, with the modeling assumptions

outlined in Chapter 2, was not able to provide adequate damping to the W-SSCI mode for reasonable BESS ratings even when the conductance of the inverter was biased using an FDVA controller. Depending on the scenario, the required BESS rating needed to stabilize the W-SSCI mode would be 4-10 times the rating of the wind plant, which is not an economically feasible solution for a number of reasons. The primary reason for this outcome is that grid-following inverters inherently exhibit very low admittance across the sub-synchronous frequency range. To enable the FDVA controller, or a similar controller which does not fundamentally change the operating characteristic of the inverter, to significantly increase the effective admittance, it would require applying a very large gain in the control loop. However, large gains were found to destabilize the inverter in other frequency regions or under large-signal disturbance conditions in this analysis. Additionally, the grid-following inverter BESS was problematic at large MW ratings because the weak system mode would become unstable, which meant that no overall stable system was found for most of the scenarios.

6.1.3 Grid-Forming BESS as W-SSCI Mitigation

The conclusions drawn from this thesis provide a strong argument for the use of grid-forming inverters for battery plants in regions which are stability-constrained due to W-SSCI. A thorough cost-benefit analysis of W-SSCI mitigation options was not performed, however the performance comparison with grid-following inverters shows the clear benefit of using grid-forming inverters and demonstrates the drawbacks of grid-following inverters for use in newly interconnecting BESS plants. Given the minor cost difference, if any, between these technologies, it is likely that choosing grid-forming inverters would be the most cost-effective W-SSCI mitigation option for the wind plant, when compared to the cost of conventional mitigation options.

6.2 Future Work

There are many opportunities for further development of the concepts presented in this thesis. These include:

- **Increased complexity of test system.** The relatively simple radial system considered in this thesis was appropriate for demonstrating and testing the basic concepts presented, however a more complex system with multiple sources of negative damping (i.e. wind plants), multiple series capacitors, and multiple grid-forming BESS plants is likely to provide further insight into the proposed concepts and potentially increase the confidence of conclusions.

- **Location of grid-forming BESS.** In this analysis, the BESS was assumed to be located with the same connection point as the wind plant. This is likely the best location for the BESS because it offsets the of negative damping at the source, however the effectiveness of the BESS at different locations in the series compensated system would provide further insight.

- **Further refinement of the FDVI controller and parameterization.** A numerical optimization technique was used to determine the FDVI controller parameters due to the complex relationship of the frequency-dependent resistance, impedance, and resulting conductance. This process may be reduced to an analytical method if the relationships between the parameters and the resultant conductance is better understood.

- **Cost-benefit analysis of GFM BESS as W-SSCI mitigation.** A cost-benefit analysis comparing classical W-SSCI mitigation solutions (or other forms of sub-synchronous instability) to new grid-forming-enabled solutions, including the BESS application mentioned here and other options such as a grid-forming STATCOM.

- **Improvement of grid-forming fault ride-through.** The grid-forming model used in this analysis was susceptible to wind-up of internal variables during the fault, leading to poor post-fault recovery performance. This portion of the model could be reviewed and improved by making use of the wealth of research on this topic.

References

[1] J. Matevosyan, J. MacDowell, N. Miller, *et al.*, "A future with inverter-based resources: Finding strength from traditional weakness," *IEEE Power and Energy Magazine*, vol. 19, no. 6, pp. 18–28, 2021. DOI: 10.1109/MPE.2021.3104075.

[2] F. Arraño-Vargas, Z. Shen, S. Jiang, J. Fletcher, and G. Konstantinou, "Challenges and mitigation measures in power systems with high share of renewables—the Australian experience," *Energies*, vol. 15, no. 2, 2022, ISSN: 1996-1073. DOI: 10.3390/en15020429. URL: https://www.mdpi.com/1996-1073/15/2/429.

[3] B. Kroposki, B. Johnson, Y. Zhang, V. Gevorgian, P. Denholm, B.-M. Hodge, and B. Hannegan, "Achieving a 100% renewable grid: Operating electric power systems with extremely high levels of variable renewable energy," *IEEE Power and Energy Magazine*, vol. 15, no. 2, pp. 61–73, 2017. DOI: 10.1109/MPE.2016.2637122.

[4] NERC, "White paper: Grid forming technology - bulk power system reliability considerations," 2021. URL: https://www.nerc.com/comm/RSTC_Reliability_Guidelines/White_Paper_Grid_Forming_Technology.pdf.

[5] A. Quedan, A. Goharrizi, Y. Cheng, S.-H. F. Huang, W. Du, and D. Ramasubramanian, "Grid-forming inverters for stability improvements in bulk power systems with high inverter-based resources penetration," in *IEEE Power and Energy Society General Meeting (PESGM)*, 2024, pp. 1–5. DOI: 10.1109/PESGM51994.2024.10688581.

[6] A. Hoke, A. Isaacs, L. Unruh, *et al.*, "White paper: Grid forming functional specifications for BPS-connected battery energy storage systems," 2023. URL: https://www.nerc.com/comm/RSTC_Reliability_Guidelines/White_Paper_GFM_Functional_Specification.pdf.

[7] P. Kundur, *Power System Stability and Control*. New York, NY, USA: McGraw-Hill, 1994.

[8] S. Muller, M. Deicke, and R. De Doncker, "Adjustable speed generators for wind turbines based on doubly-fed induction machines and 4-quadrant IGBT converters linked to the rotor," in *IEEE Industry Applications Conference*, vol. 4, 2000, 2249–2254 vol.4. DOI: 10.1109/IAS.2000.883138.

[9] J. Adams, C. Carter, and S.-H. Huang, "ERCOT experience with sub-synchronous control interaction and proposed remediation," in *PES T&D*, 2012, pp. 1–5. DOI: 10.1109/TDC.2012.6281678.

[10] Y. Cheng, L. Fan, J. Rose, *et al.*, "Real-world subsynchronous oscillation events in power grids with high penetrations of inverter-based resources," *IEEE Transactions on Power Systems*, vol. 38, no. 1, pp. 316–330, 2023. DOI: 10.1109/TPWRS.2022.3161418.

[11] G. D. Irwin, A. K. Jindal, and A. L. Isaacs, "Sub-synchronous control interactions between type 3 wind turbines and series compensated AC transmission systems," in *IEEE Power and Energy Society General Meeting*, 2011, pp. 1–6. DOI: 10.1109/PES.2011.6039426.

[12] CIGRE Joint Working Group C4/B4.52, "Guidelines for subsynchronous oscillation studies in power electronics dominated power systems," *CIGRE Technical Brochure 909*, 2023.

[13] Lawrence Berkeley National Laboratory, "Hybrid power plants: State of the market and trends," Lawrence Berkeley National Laboratory, Tech. Rep., 2023. URL: https://

emp.lbl.gov/hybrid#:~:text=At%20the%20end%20of%202023,strong%20developer%20interest%20in%20hybridization.

[14] M. Kristian and M. Prorok. "MISO interconnection rules for hybrid resources shape access to electricity market." (2020), URL: https://betterenergy.org/blog/miso-interconnection-rules-for-hybrid-resources-shape-access-to-electricity-market/.

[15] V. Sewdien, X. Wang, J. Rueda Torres, and M. van der Meijden, "Critical review of mitigation solutions for SSO in modern transmission grids," *Energies*, vol. 13, no. 13, 2020, ISSN: 1996-1073. DOI: 10.3390/en13133449. URL: https://www.mdpi.com/1996-1073/13/13/3449.

[16] A. E. Leon and J. A. Solsona, "Sub-synchronous interaction damping control for DFIG wind turbines," *IEEE Transactions on Power Systems*, vol. 30, no. 1, pp. 419–428, 2015. DOI: 10.1109/TPWRS.2014.2327197.

[17] I. Vieto, D. Howard, and S. Achilles, "Inertia contribution of a grid forming DFIG wind turbine - performance considerations and prototype demonstration results," in *22nd Wind and Solar Integration Workshop*, 2023, pp. 151–156. DOI: 10.1049/icp.2023.2731.

[18] J. L. Rodríguez-Amenedo and S. A. Gómez, "Damping low-frequency oscillations in power systems using grid-forming converters," *IEEE Access*, vol. 9, pp. 158 984–158 997, 2021. DOI: 10.1109/ACCESS.2021.3130333.

[19] J. He and Y. W. Li, "Analysis, design, and implementation of virtual impedance for power electronics interfaced distributed generation," *IEEE Transactions on Industry Applications*, vol. 47, no. 6, pp. 2525–2538, 2011. DOI: 10.1109/TIA.2011.2168592.

[20] A. Micallef, M. Apap, C. Spiteri-Staines, and J. M. Guerrero, "Performance comparison for virtual impedance techniques used in droop controlled islanded microgrids," in *International Symposium on Power Electronics, Electrical Drives, Automation and Motion (SPEEDAM)*, 2016, pp. 695–700. DOI: 10.1109/SPEEDAM.2016.7526013.

[21] A. D. Paquette and D. M. Divan, "Virtual impedance current limiting for inverters in microgrids with synchronous generators," *IEEE Transactions on Industry Applications*, vol. 51, no. 2, pp. 1630–1638, 2015. DOI: 10.1109/TIA.2014.2345877.

[22] PSCAD. "Type 3 wind turbine generators," PSCAD / Manitoba Hydro International. (2018), URL: https://www.pscad.com/knowledge-base/article/496.

[23] S. Chiniforoosh, J. Jatskevich, A. Yazdani, V. Sood, V. Dinavahi, J. A. Martinez, and A. Ramirez, "Definitions and applications of dynamic average models for analysis of power systems," *IEEE Transactions on Power Delivery*, vol. 25, no. 4, pp. 2655–2669, 2010. DOI: 10.1109/TPWRD.2010.2043859.

[24] M. Dursun and M. K. DÖŞOĞLU, "LCL filter design for grid connected three-phase inverter," in *2018 2nd International Symposium on Multidisciplinary Studies and Innovative Technologies (ISMSIT)*, 2018, pp. 1–4. DOI: 10.1109/ISMSIT.2018.8567054.

[25] P. Unruh, M. Nuschke, P. Strauß, and F. Welck, "Overview on grid-forming inverter control methods," *Energies*, vol. 13, no. 10, 2020, ISSN: 1996-1073. DOI: 10.3390/en13102589. URL: https://www.mdpi.com/1996-1073/13/10/2589.

[26] N. Mohammed, H. Udawatte, W. Zhou, D. J. Hill, and B. Bahrani, "Grid-forming inverters: A comparative study of different control strategies in frequency and time domains," *IEEE Open Journal of the Industrial Electronics Society*, vol. 5, pp. 185–214, 2024. DOI: 10.1109/OJIES.2024.3371985.

[27] B. Bahrani, M. H. Ravanji, B. Kroposki, D. Ramasubramanian, X. Guillaud, T. Prevost, and N.-A. Cutululis, "Grid-forming inverter-based resource research landscape: Understanding the key assets for renewable-rich power systems," *IEEE Power and Energy Magazine*, vol. 22, no. 2, pp. 18–29, 2024. DOI: 10.1109/MPE.2023.3343338.

[28] W. Du and S. M. Mohiuddin, "A two-stage current limiting control strategy for improved low-voltage ride-through capability of direct-droop-controlled, grid-forming

inverters," in *IEEE Energy Conversion Congress and Exposition (ECCE)*, 2023, pp. 2886–2890. DOI: 10.1109/ECCE53617.2023.10362015.

[29] Z.-l. Li, J. Hu, and K. W. Chan, "A new current limiting and overload protection strategy for droop-controlled voltage-source converters in islanded AC microgrids under grid faulted conditions," in *IEEE Energy Conversion Congress and Exposition (ECCE)*, 2020, pp. 3888–3893. DOI: 10.1109/ECCE44975.2020.9235911.

[30] PowerWorld Corporation. "Plant Controller Model: REPC_A, REPCA1 and REPCTA1." (2024), URL: https://www.powerworld.com/WebHelp/Content/TransientModels_HTML/Plant%20Controller%20REPC_A.htm.

[31] G.-C. Hsieh and J. Hung, "Phase-locked loop techniques. A survey," *IEEE Transactions on Industrial Electronics*, vol. 43, no. 6, pp. 609–615, 1996. DOI: 10.1109/41.544547.

[32] A. Y. Goharrizi, J. C. Garcia Alonso, E. Borisova, F. Mosallat, and D. Muthumuni, "Benchmark model of type-III wind turbine for research and development applications," in *IEEE Canadian Conference on Electrical and Computer Engineering (CCECE)*, 2018, pp. 1–6. DOI: 10.1109/CCECE.2018.8447781.

[33] P. Pourbeik, R. Koessler, D. Dickmander, and W. Wong, "Integration of large wind farms into utility grids (part 2 - performance issues)," in *IEEE Power Engineering Society General Meeting (IEEE Cat. No.03CH37491)*, vol. 3, 2003, 1520–1525 Vol. 3. DOI: 10.1109/PES.2003.1267381.

[34] P. Belkin, "Event of 10/22/09," 2009. URL: https://www.slideserve.com/myra-snyder/event-of-10-22-09.

[35] M. K. Das, A. M. Kulkarni, and A. M. Gole, "A screening technique for anticipating network instabilities in AC-DC systems using sequence impedances obtained by frequency scanning," in *10th IET International Conference on AC and DC Power Transmission*, 2012, pp. 1–6. DOI: 10.1049/cp.2012.1965.

[36] M. K. Das, "D-Q and dynamic phasor based frequency scanning analysis of grid-connected power electronic systems," Ph.D. Thesis, Indian Institute of Technology, Bombay, 2016.

[37] M. Shirinzad, "Frequency scan based stability analysis of power electronic systems," M.Sc. Thesis, University of Manitoba, Winnipeg, 2021.

[38] K. Dey and A. M. Kulkarni, "Passivity based grid-connectivity criterion for ensuring stability of a network with controlled power injection devices," in *IEEE Power and Energy Society General Meeting (PESGM)*, 2019, pp. 1–5. DOI: 10.1109/PESGM40551.2019.8973999.

[39] J. A. Nelder and R. Mead, "A simplex method for function minimization," *The Computer Journal*, vol. 7, no. 4, pp. 308–313, 1965. DOI: 10.1093/comjnl/7.4.308.

[40] R. L. Haupt and S. E. Haupt, *Practical Genetic Algorithms*. New York: Wiley-Interscience, 1998, ISBN: 978-0471188733.

[41] S. Shah, P. Koralewicz, E. Mendiola, V. Gevorgian, R. Wallen, and W. Yan, *Grid impedance scan tool (GIST): Software for stability analysis of IBR power systems*, 2023.

[42] S. Shah, P. Koralewicz, V. Gevorgian, and R. Wallen, "Sequence impedance measurement of utility-scale wind turbines and inverters – reference frame, frequency coupling, and MIMO/SISO forms," *IEEE Transactions on Energy Conversion*, vol. 37, no. 1, pp. 75–86, 2022. DOI: 10.1109/TEC.2021.3093516.

[43] B. Gustavsen and A. Semlyen, "Rational approximation of frequency domain responses by vector fitting," *IEEE Transactions on Power Delivery*, vol. 14, no. 3, pp. 1052–1061, 1999. DOI: 10.1109/61.772353.